ABSTRACT

Development of a Model for an Objective Minimum Resolvable Temperature Difference Characterization of an Infrared Camera

by

Christine Mourad

The parameter almost universally adopted by the infrared community for describing the overall performance of a thermal imaging camera is the minimum resolvable temperature difference. Unfortunately, this criterion is subjectively determined by a group of observers and as a consequence significantly varying results can be obtained at different times. This project describes work on an approach which ultimately aims to replace the observers by a computer-aided installation that simulates the human process by which the MRTD is estimated. The simulation is based on a direct measurement of signal to noise ratio in the image of the target and a determination of the target temperature difference which produces a signal to noise ratio equal to a pre-set threshold value. The primordial step consisted of successfully capturing a digital image in real time from a 320 X 244 CCD with Schottky-barrier detectors infrared camera. The image processing equipment needed for this task is made up of MaxVideo boards from Datacube, inc. Subjectively evaluated MRTDs at various spatial frequencies and the results obtained from this method are compared.

DEVELOPMENT OF A MODEL FOR AN OBJECTIVE MINIMUM RESOLVABLE TEMPERATURE DIFFERENCE CHARACTERIZATION OF AN INFRARED CAMERA

by
Christine Mourad

A Professional Project
Submitted to the Faculty of the
New Jersey Institute of Technology
in Partial Fulfillment of the Requirements for the
Degree of Engineer

Department of Electrical and Computer Engineering
January, 1993

Blank Page

APPROVAL PAGE

Development of a Model for an Objective Minimum Resolvable Temperature Difference Characterization of an Infrared Camera

by
Christine Mourad

Dr. Edwin Hou, Project Advisor
Assistant Professor of Electrical and Computer Engineering, NJIT

Dr. Walter F. Kosonocky
Distinguished Professor of Electrical and Computer Engineering
NJIT Foundation Chair for Optoelectronics and Solid State Circuits, NJIT

BIOGRAPHICAL SKETCH

Author: Christine Mourad

Degree: Degree of Engineer in Electrical Engineering

Date: January, 1993

Education:

* Degree of Engineer in Electrical Engineering
  New Jersey Institute of Technology, Newark, NJ, 1993

* Master of Science in Electrical Engineering
  New Jersey Institute of Technology, Newark, NJ, 1988

* Bachelor of Science in Electrical Engineering, Tulane University
  New Orleans, LA, 1985

Major: Electrical Engineering

Dedicated to the memory of my beloved grandparents

ACKNOWLEDGMENT

TABLE OF CONTENTS

LIST OF TABLES

LIST OF FIGURES

Figure

CHAPTER 1

INTRODUCTION

The objective of this project was to develop and implement a computer-aided methodology to objectively measure the minimum resolvable temperature difference (MRTD) of a thermal imaging camera. The infrared camera used throughout this study was developed at the David Sarnoff Research Center in Princeton, NJ [1].

Chapter 2 contains the necessary basic concepts of optical geometry. Chapter 3 expands on the radiometric concepts underlying the fundamentals of signal integration by the 320 X 244 infrared charge coupled device with Schottky barrier detectors imager (IR-CCD with SBD). Chapter 4 provides a description of the RS-170 video standard, including the timings of the various synchronization and blanking pulses. Chapter 5 describes the MRTD concept, the standard test used, and the method implemented in this work. Appendices A through C contain the listings of the various software developed throughout this work.

CHAPTER 2

OPTICAL GEOMETRY FUNDAMENTALS

2.1 Spherical Coordinates

The most useful coordinate system for optical radiation measurements is the spherical one, since what is needed are coordinates that can specify the direction of a ray in or out of the hemisphere enclosing the plane tangent to the reference surface dA. The spherical coordinate system is shown in Figure 2.1. The tangent plane containing the infinitesimal area element dA is chosen as the x-y plane and the normal to dA as the polar axis for spherical coordinates and equivalently as the z-axis for rectangular coordinates. As shown in Figure 2.1 the spherical coordinates of any point in space (P) are then ρ, θ, ϕ, where ρ is the length of the line OP, θ is the polar angle between the line OP and the polar axis z, and ϕ is the azimuth angle which is the angle between the projection of OP on the tangent plane and the azimuth reference (x-axis). The relationships between rectangular and spherical coordinates are summarized in the following set of equations.

$$x = \rho \cdot \sin\theta \cdot \cos\phi$$

$$y = \rho \cdot \sin\theta \cdot \sin\phi \qquad \text{and} \qquad (2.1)$$

$$z = \rho \cdot \cos\theta \ .$$

$$\rho = \left(x^2 + y^2 + z^2\right)^{1/2} \qquad \theta = \tan^{-1}\left[\frac{\left(x^2 + y^2\right)^{1/2}}{z}\right] \qquad \phi = \tan^{-1}\left(\frac{y}{x}\right). \qquad (2.2)$$
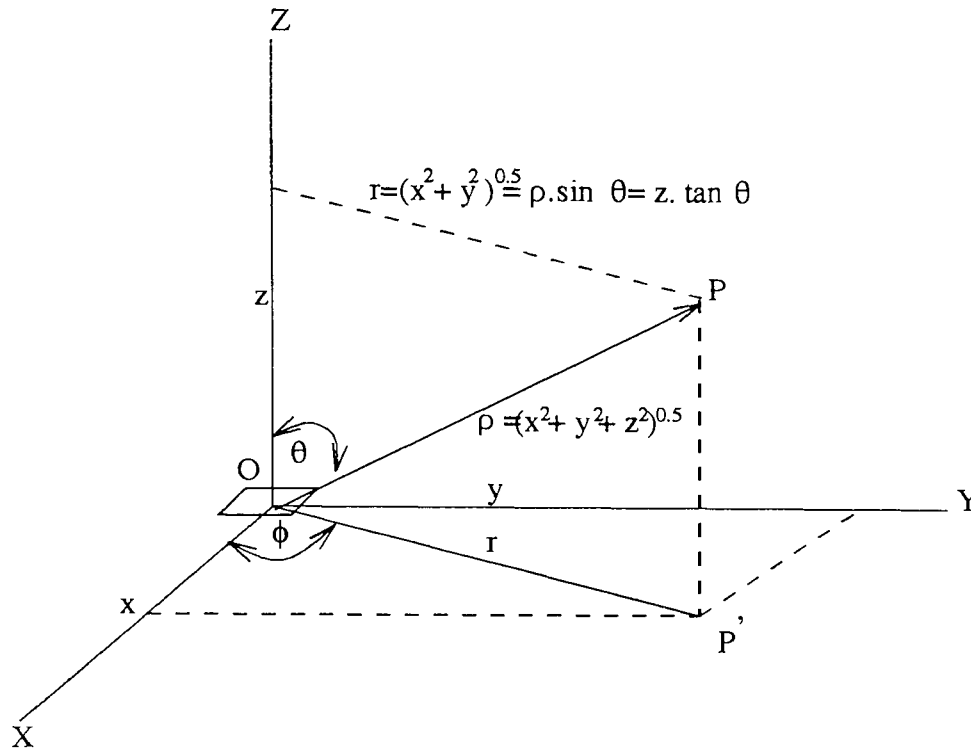
Figure 2.1 Spherical and rectangular coordinates of P (ρ, θ, ϕ) = P(x, y, z).

2.2 Solid Angle

A solid angle is formed at the vertex of a conical surface or cone. The cone, in turn, is the surface that contains all possible straight lines that extend from the vertex point to a point on some closed curve in space that does not pass through the vertex. Such a curve in the broadest sense possible can include straight lines and discontinuous changes in direction or angles. See Figure

2.2 which depicts a solid angle formed by the straight lines joining the vertex to a randomly shaped closed curve. However, a solid angle is typically represented bounded by a right circular cone.
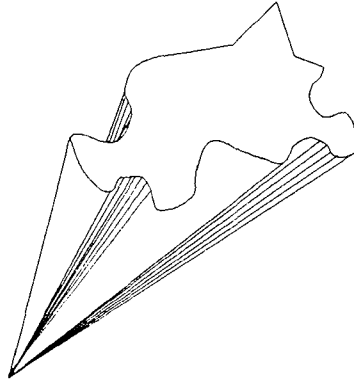
Figure 2.2 A Solid Angle.

The measure of a solid angle is given by the area intercepted by the bounding cone, on the surface of a sphere centered at its vertex. The magnitude of a solid angle ω is given by the ratio of the intercepted spherical- surface area A_s to the square of the radius ρ of the sphere. The unit of a solid angle is the steradian [sr].

$$\omega = A_s/\rho^2 \quad [sr] \tag{2.3}$$

It is common to use this definition of a solid angle to obtain a value for the angular subtense of any surface of area A at distance ρ^2. In most practical problems, this is a justifiable approximation since ρ^2 is much larger than A.

2.2.1 The Solid Angle in Spherical Coordinates

Consider the incremental angle $d\theta$ which intercepts an arc of length $\rho d\theta$ on a spherical surface centered on O with a radius ρ as shown in Figure 2.3.
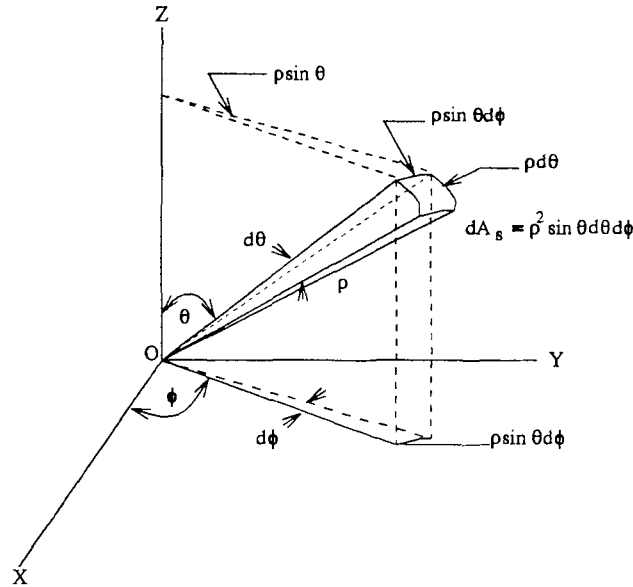
Figure 2.3 An Element of Solid Angle $d\omega = dA_s/\rho^2 = \sin\theta \, d\theta \, d\phi$.

The incremental angle $d\phi$ intercepts an arc of radius $\rho \sin\theta$. The length of that circular arc on the spherical surface is then the product of that radius by the infinitesimal angle $= \rho \sin\theta \, d\phi$. Both arcs form an element of the spherical surface $dA_s = \rho^2 \sin\theta \, d\theta \, d\phi$. Therefore, from equation 2.3:

$$d\omega = dA_s/\rho^2 = \sin\theta \, d\theta \, d\phi \quad [\text{sr}] \qquad (2.4)$$

It is evident that since the angle elements $d\theta$ and $\sin\theta \, d\phi$ are in radians that a steradian is a square radian. The integral of an elemental solid angle (equation 2.4) gives a general expression of a solid angle in spherical coordinates:

$$\omega = \int_\phi \int_\theta \sin\theta \, d\theta \, d\phi \qquad [\text{sr}] \qquad (2.5)$$

For a spherical surface intersected by a right circular cone symmetric about the z axis the solid angle double integral is found to be equal to:

$$\omega = \int_0^\theta \int_0^2 \pi \sin\theta \ d\theta \ d\phi = 2\pi \left[1 - \cos\theta\right] \qquad (2.6)$$

When the associated cone subtends a plane angle of 2θ $(0 \leq \theta \leq \pi/2)$, ie., the solid angle is at the vertex of a hemisphere, it has a value of of 2π. Similarly, when the solid angle subtends a spherical surface, its numerical value is of 4π.

The general case of an element of solid angle $d\omega_{12}$ subtended at a surface dA_1 by an arbitrarily oriented area element dA_2 at a distance of D is shown in Figure 2.4. It is obvious that the incremental solid angle intercepts an area element $dA_2 \cos\theta_2$, which results in the following expression:

$$d\omega_{12} = \frac{dA_2 \cos\theta_2}{D^2} \quad [sr] \qquad (2.7)$$
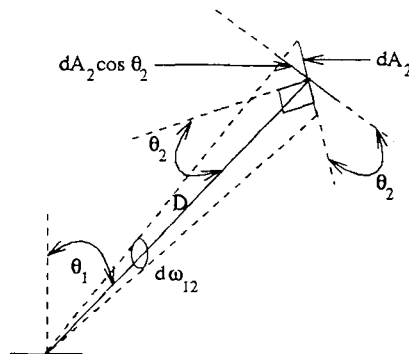
Figure 2.4 A Solid Angle Element Subtends an Arbitrarily Oriented Surface Element.

2.2.2 The Projected Solid Angle

In chapter 3, the photon-flux sterance (radiance) was defined in terms of the element of flux through a projected area $\cos\theta \ dA$ and the incremental solid angle $d\omega$. It is useful to associate the cosine term with the solid angle element as $\cos\theta \ d\omega$ and by definition call

$$\Omega \equiv \int_\omega d\Omega \equiv \int_\omega \cos\theta \ d\omega \quad [sr] \tag{2.8}$$

the projected solid angle associated with ω. Another terminology for this expression is the weighted solid angle, with $\cos\theta$ as the weighting function. The projected solid angle formulae for some useful geometries are given in the next figure.
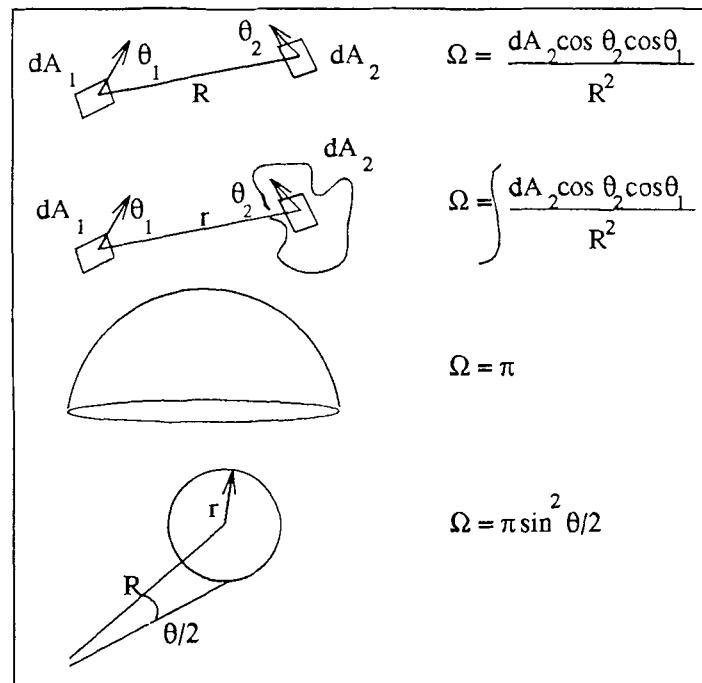
Figure 2.5 Some Useful Weighted Solid Angle Formulae.

CHAPTER 3

RADIOMETRIC PRINCIPLES

This chapter defines radiometry, its underlying concepts, and describes the calculations necessary for the characterization of detector performance and the prediction of signal and noise levels. By definition, radiometry relates to the detection and measurement of radiated electromagnetic energy, but in a broader sense it is used to describe the calculation of the power transferred from one object to another. A detailed and complete study of the measurement of optical radiation is made in [2].

3.1 Description of Optical Radiation

Electromagnetic waves lying between x-rays and microwaves, i.e., in the interval between one nanometer and one millimeter, are referred to as optical radiation. The most familiar portion is visible light, which lies approximately between 400 and 700 nanometers. Only approximate boundaries exist between the various spectrum regions as shown in Figure 3.1.

OPTICAL RADIATION

GAMMA RAYS	X-RAYS	ULTRA VIOLET	VISIBLE	INFRARED	MICROWAVE	RADIO WAVE

$$10^{-12} \quad 10^{-10} \quad 10^{-8} \quad 10^{-6} \quad 10^{-4} \quad 10^{-2} \quad 10^{+2} \quad [m]$$
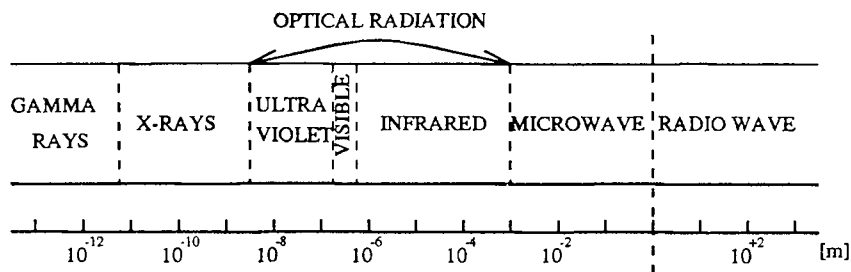
Figure 3.1 Spectrum of Electromagnetic Waves.

Since we are dealing with radiation emitted by incoherent sources then the radiometric calculations are adequately approached through geometrical optics. Optical radiation measurements involve a radiation beam starting at a source, propagating along an optical path and finally received at a radiometric instrument. The source itself can be a radiating source, or it can be an object that reflects or scatters some incident radiation emitted by another source. The propagation path might consist of different media including vacuum and might be affected by any of the following physical phenomena: reflection, refraction, absorption, scattering and emission. As for the radiometric instrument it can take a variety of forms, from the simplest photocell to the most involved spectroradiometer.

3.2 Optical Radiation Transfer

In this section, the basic radiometric concepts are introduced and explained from the spatial point of view. Note that in this thesis, radiometric relations are given in terms of photon-flux, with the radiant equivalent given for some formulae and expressions. The most fundamental radiometric quantity on which all others are based is the spectral sterance $L(\lambda, T)$. This expression is used to quantify the notion of photon (or radiant) flux per unit area, per unit solid angle, and per unit bandwidth of wavelength. All other radiometric concepts can be considered as integrals of spectral sterance over area, solid angle or wavelength.

The various radiometric quantities are given in Table 3.1 along with their units and relationships.

Table 3.1 Photon-Flux Radiometric Nomenclature.

Quantity	Symbol	Definition	Units
Photon Energy	Q_p		q (quantum)
Photon Flux	Φ_p	$\dfrac{dQ_p}{dt}$	$q.\sec^{-1}$
Photon Intensity	I_q	$\int L_q dA$	$q.\sec^{-1}.sr^{-1}$
Photon Excitance(source)	M_q	$\int L_q \cos\theta\, d\omega$	$q.\sec^{-1}.m^{-2}$
Photon Irradiance(detector)	E_q	$\int L_q \cos\theta\, d\omega$	$q.\sec^{-1}.m^{-2}$
Photon Sterance	L_q	$\dfrac{d^2\Phi_q}{dA\cos\theta\, d\omega}$	$q.\sec^{-1}.m^{-2}.sr^{-1}$
Spectral Photon Sterance	$L_{q,\lambda}$	$\dfrac{dL_q}{d\lambda}$	$q.\sec^{-1}.sr^{-1}.m^{-2}.nm^{-1}$
Spectral Photon Energy ***	$Q_{q,\lambda}$	$\dfrac{dQ_q}{d\lambda}$	$q.nm^{-1}$.

*** Other spectral quantities are treated similarly.

3.2.1 The Concept of Sterance

Consider the setup in Figure 3.2, whereby the flux $\Delta\Phi$ is measured at the detector. It is found that the measured flux depends on the areas of the source and detector , the distance between them, their tilt with respect to the normals and the "brightness" L of the source. The incremental flux throughout the entire spectrum is given by:

$$\Delta\Phi = \frac{(\varepsilon \Delta A_s \cos\theta_s)\,(\alpha\,\Delta A_d \cos\theta_d)}{r^2}\,\tau\;L(T) \tag{3.1}$$

where the total sterance is related to the spectral quantity by the integral over all wavelengths:

$$L(T) = \int_0^\infty L(\lambda, T)d\lambda$$

The symbols introduced in this primary equation are listed next [3]:

- ε: emissivity of source

$$\varepsilon = \begin{cases} 1.000 & \text{for a perfect emitter} \\ 0.995 & \text{for specially treated black cavities} \\ 0.02 & \text{for some gold-plated surfaces} \end{cases}$$

- $\Delta A_s, \Delta A_d$: infinitesimal source , receiver areas.

- θ_s, θ_d: tilt angle of source, receiver, i.e. : angle between the normal to the respective surfaces and the direction of r.

- α: absorptivity of receiver

$$\alpha = \begin{cases} 1.000 & \text{for a perfect absorber} \\ 0.995 & \text{for specially treated black cavities} \\ 0.02 & \text{for some gold-plated surfaces} \end{cases}$$

- $L(\lambda, T)$: spectral photon-flux sterance of the source at

  temperature T, wavelength λ.

- r: distance between source and receiver.

- τ: transmittance factor for all components between the source and receiver.
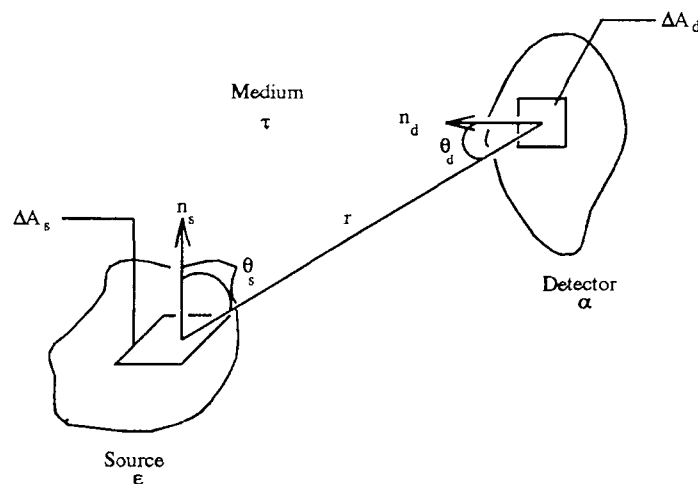
Figure 3.2 Radiation Exchange Between Elemental Surfaces ΔA_s, ΔA_d.

Solving the power transfer equation for L, and taking the limit of L as

ΔA_s, ΔA_d go to zero provides the following definition for L:

$$L(T) = \lim_{\substack{\Delta A_d \to 0 \\ \Delta A_s \to 0}} \frac{\Delta \Phi}{(\Delta A_s \cos \theta_s \Delta A_d \cos \theta_d)/r^2} = \frac{d^2 \Phi}{dA_s dA_d \dfrac{\cos \theta_s \cos \theta_d}{r^2}}$$

where $(\Delta A_d \cos\theta_d)/r^2$ is the solid angle subtended at the source by the receiver therefore the defining equation forthe sterance becomes

$$L(T) = \frac{d^2\Phi}{dA \cos\theta\, d\omega}\,. \tag{3.2}$$

3.2.3 Cosine Law of Radiometry

The cosine law of radiometry can be derived from equation 3.1 and from the geometry illustrated in Figure 3.3, which gives the various possible configurations between a source and a detector [4]. As shown in the diagram, the distance between the source and the detector planes in cases 1, 2 & 3 is R , while for cases 4 and 5 the distance is $R' = \dfrac{R}{\cos\theta}$.

For simplicity, let α , ε and τ all be 1.

In case 1, $\Delta\Phi = \dfrac{L\Delta A_s \Delta A_d}{R^2}$.

In case 2, $\Delta\Phi = \dfrac{L\Delta A_s \Delta_d}{R^2} \cos\theta$.

In case 3, $\Delta\Phi = \dfrac{L\Delta A_s \Delta_d}{R^2} \cos^2\theta$.

Substituting R' by $R/\cos\theta$ in case 4 leads to

$$\Delta\Phi = \frac{L\Delta A_s \Delta_d}{R'^2} \cos\theta = \frac{L\Delta A_s \Delta_d}{R^2} \cos^3\theta$$

And in case 5 to : $\Delta\Phi = \dfrac{L\Delta A_s \Delta_d}{R'^2} \cos^2\theta = \dfrac{L\Delta A_s \Delta_d}{R^2} \cos^4\theta$
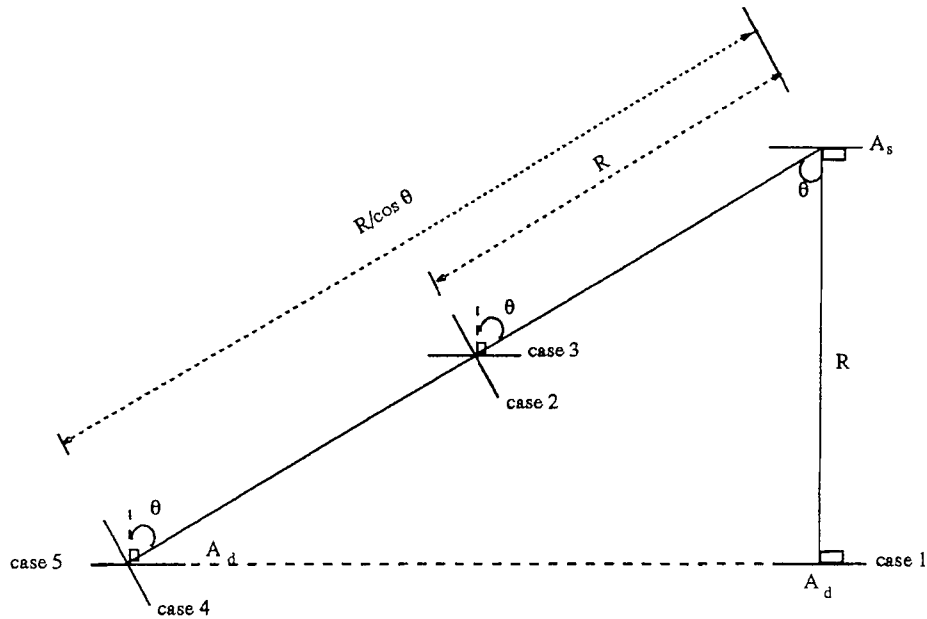
Figure 3.3 Geometry of the Cosine Law of Radiometry.

The cosine factors as evidenced in the above expressions accumulate to include area projection and distance-increase effects. It is evident from case 5, that the signal across the detector plane varies as the fourth power of the cosine of the off-axis angle. The generalized cosine dependence can be summarized as follows

$$\Delta\Phi = \frac{L\Delta A_s \Delta A_d}{R^2} \cos^{n-1}\theta, \text{ where n is the case number.} \qquad (3.3)$$

As an illustration of the applicability of the cosine law on real life situations, consider the irradiation on a detector plane focused by a perfect lens free of aberrations and defects, which will transmit all the incident radiation on it (see Figure 3.4). The flux incident on the lens is then given by the cosine law (n = 5), with the detector area ΔA_d replaced by the lens area A_l.

At the detector plane, the average irradiance is given by the ratio of the incident power to the area of the detector:

$$E = \frac{\Delta\Phi}{\Delta A_d} = \frac{L\Delta A_s A_l}{\Delta A_d R^2}\cos^4\theta .$$

The solid angle ω subtended by the detector at the lens is equal to the solid angle subtended by ΔA_s at the lens, where:

$$\omega = \frac{A_d}{f^2} = \frac{A_s}{R^2} .$$

using the previous equality in the expression for the plane irradiance leads to the following equation:

$$E = \frac{L\Delta A_d A_l}{\Delta A_d f^2}\cos^4\theta = \frac{LA_l}{f^2}\cos^4\theta .$$
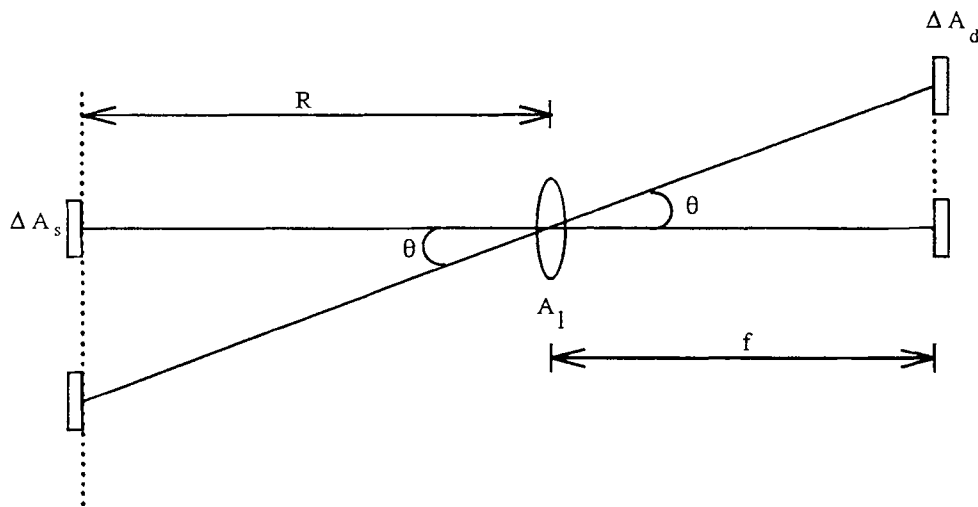
Figure 3.4 Detector Plane Irradiance.

3.2.2 Lambertian Radiators

Many actual radiation sources can be approximated as Lambertian radiators, and an analysis of its properties will lead to an important radiometric identity that relates sterance to excitance. The sterance of such a surface is independent of the angle from where it is viewed, i.e., it has the same value in all directions from the surface. The power incident on a spherical surface element dA of the hemisphere in Figure 3.5 is

$$d\Phi = \frac{L \, dA_s \cos\theta \, dA}{r^2} = \frac{LdA_s \cos\theta \, r \sin\theta \, d\theta \, r \, d\phi}{r^2}$$

$$= LdA_s \cos\theta \, \sin\theta \, d\theta \, d\phi.$$

The total excitance M on the hemisphere can be found as follows:

$$M = \int_{hemisphere} \frac{d\Phi}{dA_s} = L \int_o^{\pi/2} \int_0^{2\pi} \cos\theta \, \sin\theta \, d\theta \, d\phi.$$

The result of the above integration is

$$M = \pi L. \tag{3.4}$$
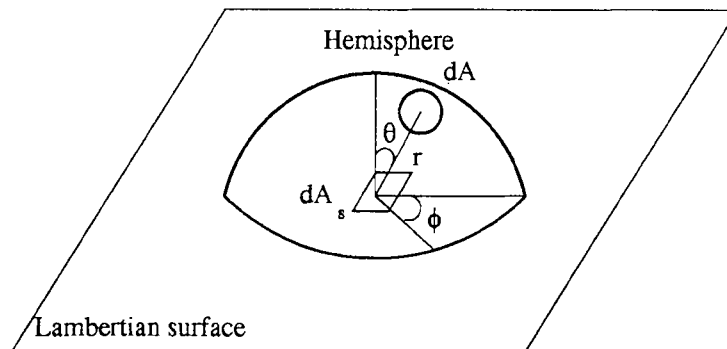
Figure 3.5 Lambertian Source.

3.3 Spectral Content

A good understanding of the laws of thermal radiation is necessary for making radiation measurements. The fundamental relation is Planck's radiation law for spectral sterance.

3.3.1 Blackbody Radiation

The concept of a blackbody is important when trying to describe power transfer from one object to the other. By definition, a blackbody is an idealized element that absorbs all incident radiation on it (no reflection or transmission of energy). This ideal body therefore, is completely opaque and non-reflecting in all directions and at all wavelengths. Such an object at equilibrium and at an absolute temperature $T(K)$, radiates uniformly according to Planck's radiation law

$$L_q(\lambda, T) = \frac{2c}{\lambda^4 \left(e^{hc/\lambda kT} - 1 \right)} \quad \left[\text{photons/(cm}^2 \cdot \mu\text{m}) \right], \qquad (3.5a)$$

$$L_e(\lambda, T) = \frac{2hc^2}{\lambda^5 \left(e^{hc/\lambda kT} - 1 \right)} \quad \left[\text{W/(cm}^2 \cdot \mu\text{m}) \right], \qquad (3.5b)$$

where

c is the velocity of light in a vacuum $\approx 2.998 \times 10^{10} \text{cm} \cdot \text{sec}^{-1}$

h is Planck's constant $= 6.626 \times 10^{-34} \text{J} \cdot \text{sec}$

k is Boltzmann's constant $= 1.381 \times 10^{-23} \text{J/K}$

Manipulating equations (3.5a) and (3.5b) leads to the following identity

$$L_e(\lambda, T) = L_q(\lambda, T) \frac{hc}{\lambda}$$

The above equations are easily evaluated but two limiting cases are useful in producing approximate results. Substituting $\frac{hc}{\lambda kT}$ by x in equation (3.5b) yields the following expression for photon-flux sterance:

$$L_q(x, T) = \left[\frac{2(kT/h)^4}{c^3} \right] \left[\frac{x^4}{e^x - 1} \right].$$

• At short wavelengths (high frequencies), where $e^x \gg 1$, the following approximation $\frac{x^4}{e^x - 1} \approx \frac{x^4}{e^x}$ holds true thus leading to Wien's radiation law. A similar approximation yields the power spectral sterance L_e analog.

$$L_q(\lambda, T) \approx \left(\frac{2c}{\lambda^4} \right) e^{-(hc/\lambda kT)},$$

$$L_e(\lambda, T) \approx \left(\frac{2hc^2}{\lambda^5} \right) e^{-(hc/\lambda kT)}.$$

• At long wavelengths ($e^x \ll 1$) Planck's radiation law can be approximated by the Rayleigh-Jeans law, which is obtained by using the series expansion for $(e^x - 1) = x + \frac{x^2}{2!} + \frac{x^3}{3!} + \cdots \approx x$. The Planck radiation laws can be simplified to the following forms:

$$L_q(\lambda, T) \approx \left(\frac{2kT}{h} \right) \lambda^{-3},$$

$$L_e(\lambda, T) \approx (2ckT)\lambda^{-4} \ .$$

An ideal blackbody is a Lambertian radiator therefore, the sterance L and the excitance M of such a source are connected by the relationship $M = \pi L$ as determined in the previous section. Since excitance is the more prevalent quantity, the rest of the analysis uses it exclusively. The total amount of emission within the entire spectrum is found by integrating the spectral power (M_e) or photon-flux excitance (M_q) over all wavelengths:

$$M_q(T) = \int_0^\infty M_q(\lambda, T)d\lambda = \sigma_q T^3 \quad \left[\text{photons} \cdot \text{sec}^{-1} \cdot \text{cm}^{-2} \right], \tag{3.6a}$$

$$M_e(T) = \int_0^\infty M_e(\lambda, T)d\lambda = \sigma_e T^4 \quad \left[W \cdot \text{cm}^{-2} \right], \tag{3.6b}$$

where $\sigma_{e,q}$ are respectively the Stefan-Boltzmann constant and its photon analog.

$$\sigma_e = \frac{2\pi^5 k^4}{15 h^3 c^3} \quad , \quad \sigma_q = \frac{4\pi^4 k^3}{25.79436 h^3 c^2} \ .$$

The resulting equations are known as the Stefan-Boltzmann laws for total blackbody excitance. To find the excitance existing within a spectral band then the calculations are best done with an appropriate numerical integration routine, or with the help of preexisting tables (see Appendix C). Since $\int_{\lambda_1}^{\lambda_2} M(\lambda, T)d\lambda = \int_0^{\lambda_2} M(\lambda, T)d\lambda - \int_0^{\lambda_1} M(\lambda, T)d\lambda$ then to obtain the excitance between two wavelengths, the corresponding entries are subtracted, i.e.:

$$M(\lambda_1 \text{to} \lambda_2) = M(0 \text{ to } \lambda_2) - M(0 \text{ to } \lambda_1).$$
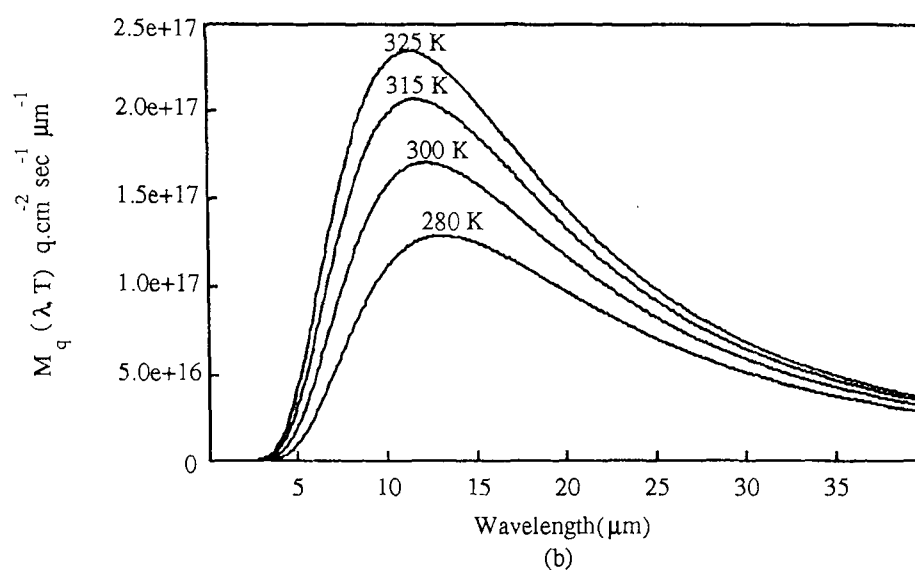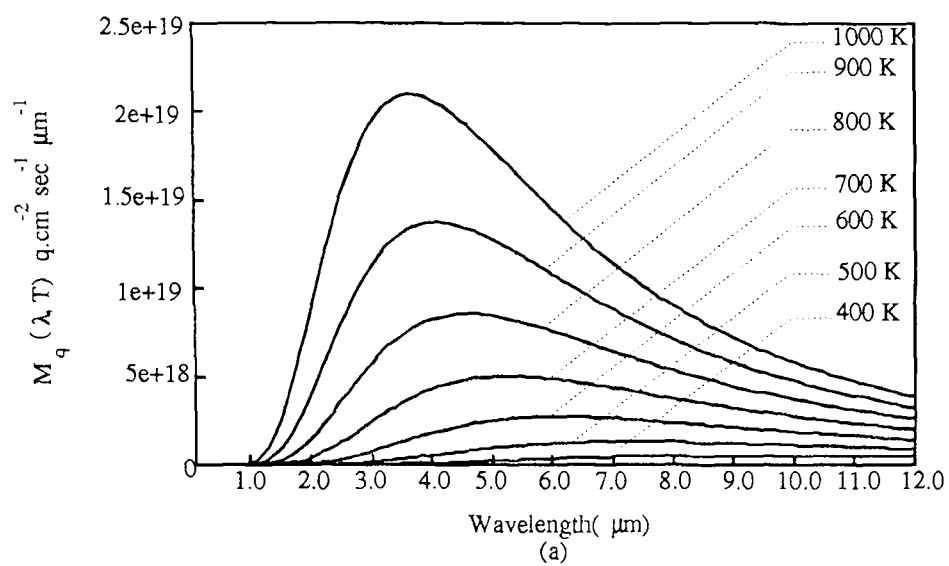
Figure 3.6 Photon Spectral Excitance for

(a)$0 < \lambda \leq 12$ and $400K \leq T \leq 1000K$

(b) $0 < \lambda \leq 40$ and T Around Room Temperature.
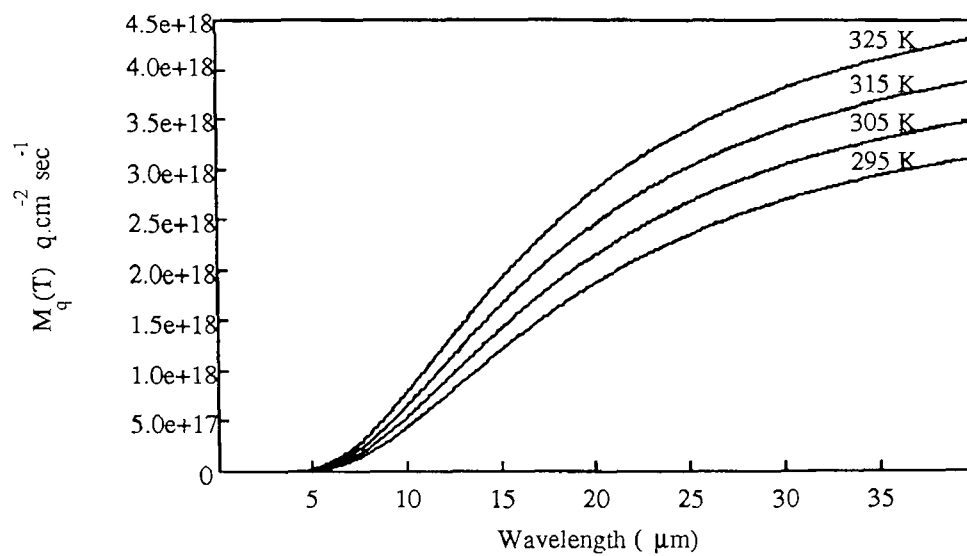
Figure 3.7 Photon Excitance for $0 < \lambda \leq 40$ and T Around Room Temperature.

CHAPTER 4

VIDEO SIGNAL SCANNING AND SYNCHRONIZATION

This chapter provides a description and analysis of video signals [5] focusing on the definition of the synchronization pulses due to their primordial role in the interface between the IR camera and the Max-Scan input board.

4.1 Fundamentals of Scanning

The rectangular area scanned by the electron beam as it is deflected horizontally and vertically is called the raster. The picture is reproduced on the raster and the scanning mechanism is linear in order to have a faithful reproduction of the picture elements.

4.1.1 Linear Scanning

Consider the following sawtooth current waveform which flows through the deflection coils in the yoke on the neck of the picture tube.
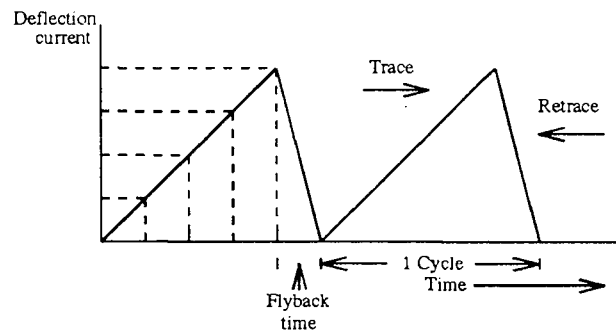
Figure 4.1 Sawtooth Scanning Waveform.

The linear rise of current in the horizontal deflection coils moves the electron beam across the screen in a continuous, uniform motion for the trace phase from left to right. When the maximum is reached, the sawtooth wave decreases rapidly to its initial value. This fast reversal produces the retrace or flyback. Horizontal trace starts at the left edge of the raster and ends at the right edge at which point the flyback produces the retrace back to the left edge. See Figure 4.2(a).
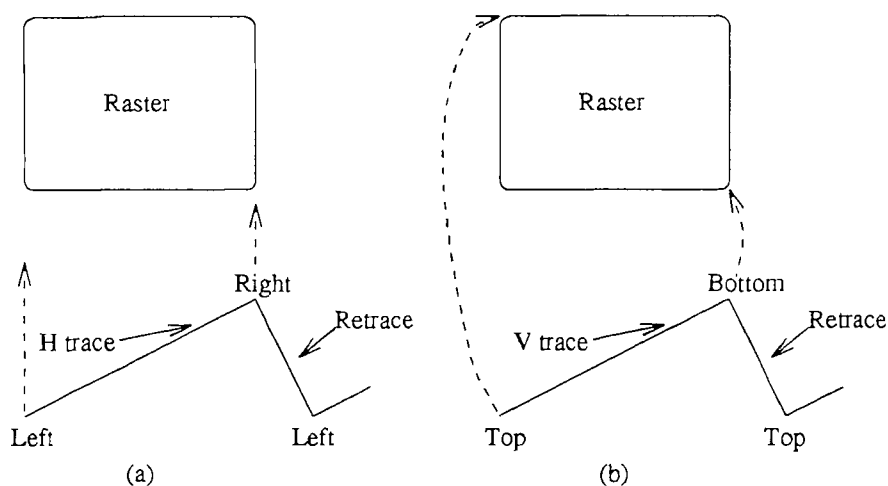
Figure 4.2 Directions for Trace and Retrace: (a) Horizontal; (b) Vertical.

Similarly, this waveform in the vertical deflection coils moves the beam from the top to the bottom of the raster with uniform speed. As such, the beam movement produces complete horizontal lines, one under the other. The trace part as indicated in Figure 4.2(b) deflects the beam towards the bottom of the raster, while the retrace part rapidly returns the beam to the top left edge of the raster.

During both the vertical and horizontal flyback intervals, all picture information is blanked out. To minimize the loss of picture information during the retrace part, the corresponding time intervals on the sawtooth waveforms are made as short as possible. Typical horizontal retrace time is approximately ten percent of the total line period, and vertical flyback time is usually about five percent of one complete cycle.

4.1.2 Standard Scanning Pattern

The scanning procedure that is used universally consists of the following steps: First all the odd lines are scanned from the top to the bottom of the frame while skipping over the even lines. After this scanning cycle, the vertical retrace period occurs which brings back as described previously the electron beam to the top of the frame. Finally all the omitted even lines are scanned from top to bottom.

Each frame is hence divided into two fields, one odd and one even. The first and all odd fields contain the odd lines of the frames while the second and all subsequent even fields contain the even scanning lines. The FCC scanning specifications provide a standard scanning pattern which includes 525 lines in a rectangular frame of aspect ratio 4 to 3. The standard frame rate is 30 frames per second. Since each frame consists of two interlaced fields, the field repetition rate is thus 60 per second and the vertical scanning frequency is 60 Hz. This scanning scheme is illustrated in Figure 4.3.
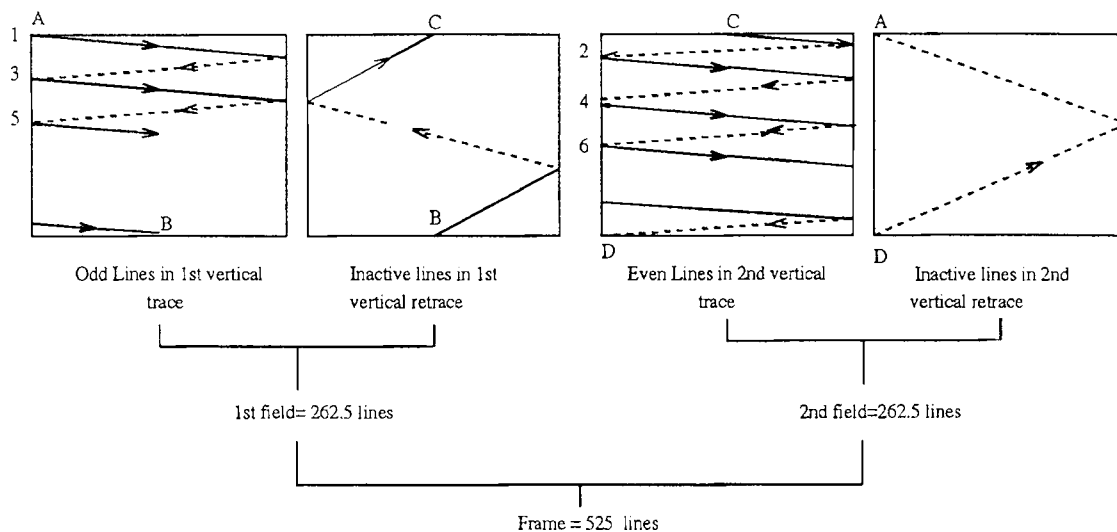
Figure 4.3 Odd-Line Interlaced Scanning Procedure.

Starting at point A, the electron beam sweeps the across the frame with uniform velocity to cover all the picture elements in one horizontal line, then retraces to the left side of the frame (the retrace part is shown in dashed lines). Note that the vertical scanning motion produces the downward inclination of the horizontal lines, but that the slope of the trace part is greater than the retrace. The reason for that discrepancy is that the faster retrace does not allow the beam as much time to deflect vertically. As seen in Figure 4.3 the beam scans line 3 omitting the second line, thus the electron beam scans all odd lines and finally reaching position B at the bottom of the frame, at which point the vertical retrace begins. The beam is brought back to the top of the frame to start the even field from point C. The several lines scanned during the vertical retrace time are not visible, because the electron beam is cut off by the blanking voltage during the flyback interval. The

second field starts at the middle of a horizontal line since the first field contained 262.5 lines. After scanning the first half-line the beam scans line 2, then continues scanning between the odd lines to produce the even numbered lines of the second field, and finally coming down to the bottom of the frame at point D which is located at a half line distance from point B.

4.1.3 The Synchronizing Pulses

To reassemble at the receiver the picture elements in the same positions as the image at the camera tube, an appropriate synchronizing pulse is transmitted for each line to keep the horizontal scanning synchronized, and a vertical synchronizing pulse is transmitted for each field to synchronize the top to bottom scanning motion. The horizontal pulses have the same frequency as the horizontal scanning , i.e 15,750 Hz and the frequency of the vertical synchronizing pulses is appropriately 60 Hz. The synchronizing pulses are sent during the blanking periods when no picture information is transmitted. This is appropriate since these pulses start the retrace intervals. The term sync is often used for brevity's sake.

The synchronizing pulses do not produce scanning, but enable the picture information reproduced on the raster to hold still in the correct position. Without V sync, the picture reproduced appears to roll up or down the raster, and without H sync the picture drifts to the left or right and then breaks into diagonal strips. As illustrated in Figure 4.4, the sync pulses consist of

horizontal pulses, a group of equalizing pulses, and vertical sync pulses. Each vertical sync extends over a period of three lines and comprises six pulses separated by five serrations at half-line intervals. The equalization pulses are used to insure identical waveshapes for the separated vertical syncs and thus constant timing for proper odd-even interlacing.
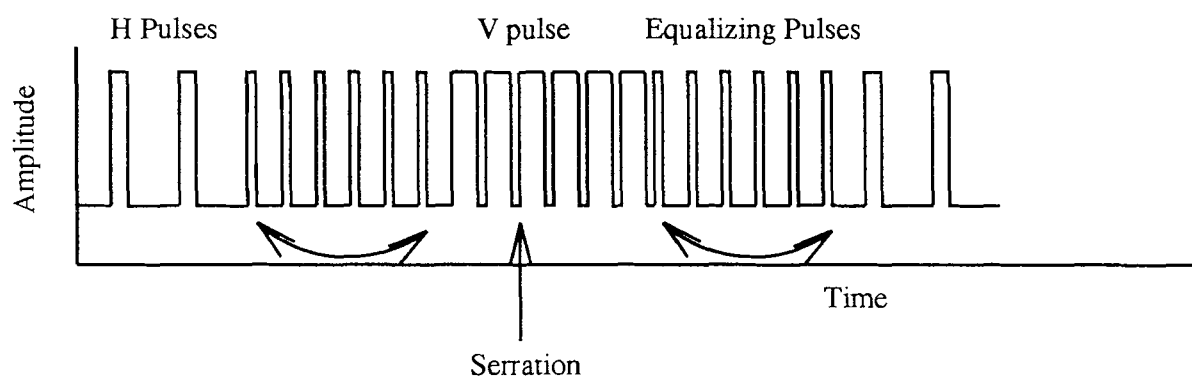
Figure 4.4 The Synchronizing Pulses.

The sync and blanking pulses have the same frequency as their scanning counterparts. For instance, the scanning waveform for vertical deflection has a 60 Hz frequency because of the V sync pulses repeated every 1/60 sec. The vertical retrace triggered by the sync pulse occurs during the blanking pulse time interval and is thus blanked out. The groups of equalizing pulses are repeated every 1/60 s but each of the pulses is spaced at half-line intervals with the frequency 31,500 Hz. As stated previously, the function of these pulses is to equalize the vertical synchronization in even and odd fields for good interlace. The frequencies are tabulated in Table 4.1.

Table 4.1 Scanning, Synchronizing, and Blanking Frequencies.

Frequency	Application
60	V sync to time V field scanning
60	V scanning to makes lines fill raster
60	V blanking to blank out V retraces
15,750	H sync to time H scanning
15,750	H scanning to produce lines
15,750	H blanking to blank out H retraces
31,500	Equalizing pulses

4.2 Composite Video Signal

This section deals with the final camera signal incorporating (a) the sync pulses used to synchronize the transmitter and receiver, (b) the blanking pulses as well as (c) the actual picture information. How these three components are added to form the composite video signal is illustrated in Figure 4.5, which shows the corresponding details for two horizontal lines. The lower 75% of the range is used for camera signal while the upper 25% is occupied by the sync pulses. Higher amplitudes correspond to darker pixels.
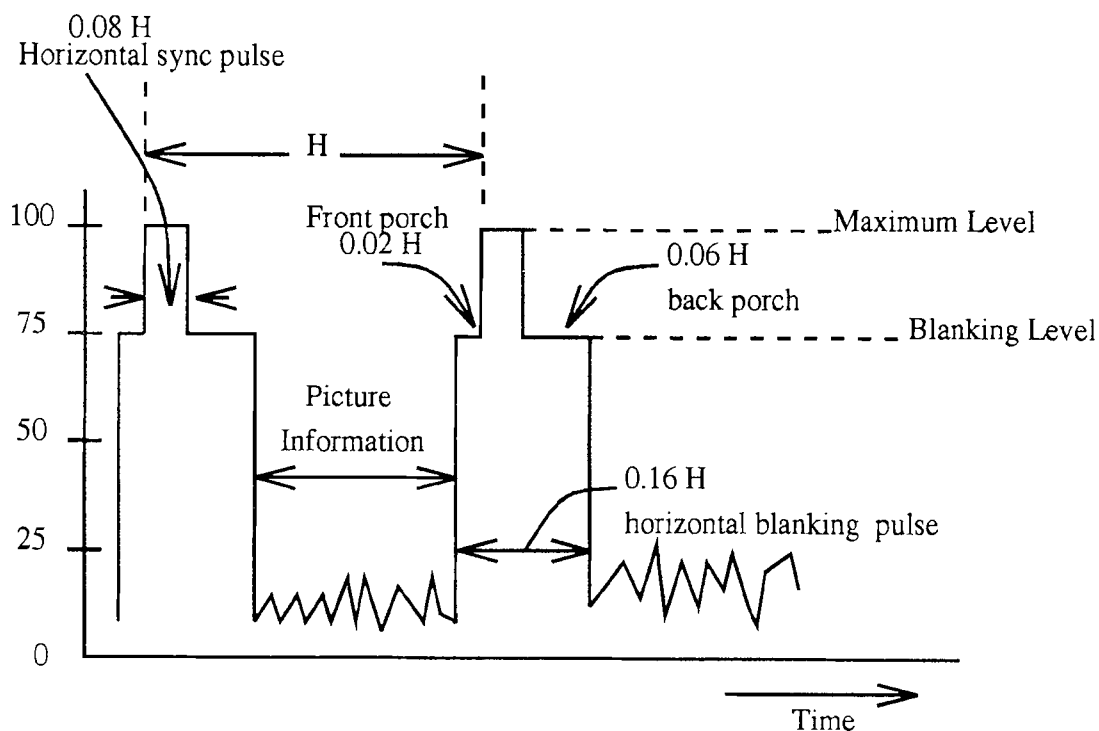
Figure 4.5 Composite Video Signal Details for Two Lines.

The composite video signal contains blanking pulses that render the retrace lines invisible by raising the signal amplitude to black level (i.e 75%) during the time that the scanning circuits produce retraces. All picture information is eliminated during the blanking time because of the black level. There are vertical and horizontal blanking pulses in the composite video signal. The horizontal blanking pulses have the function of blanking out the retrace from the right edge of the raster to the left for each line scanned. Their vertical counterparts blank out the scanning lines produced during the vertical flyback scan.

The time interval between horizontal scanning lines (including trace and retrace)is indicated by H in Figure 4.5. This is the total time needed to scan one complete line and is equal to 1/15,750(Hz) or 63.5 μs. The pertinent time interval values as depicted in the previous figure are summarized in Table 4.2.

Table 4.2 Details of Horizontal Blanking.

Interval	Time
Total line	H 63.5 μs
H blanking	0.16H 10 μs
H sync pulse	0.08H 5 μs
Front porch	0.02H
Back porch	0.06H

Blanking time is slightly longer than typical retrace values, which depend on the actual horizontal deflection circuits at the receiver. As a result, a small part of the trace is blanked out at the beginning and end of every scanning line. This effect produces black bars at the left and right sides of the raster. Horizontal retrace starts with the leading edge of the sync pulse, therefore as the scanning beam is completing its trace to the right, the blanking level of the front porch blanks out the right edge of the line thus creating a "black bar". A similar effect occurs at the left edge of the raster with the

beginning of the trace blanked out by a portion of the backporch.

The vertical blanking pulses raise the video signal amplitude to black level so that the scanning beam is blanked out during vertical retraces. The width of the blanking pulse varies between 5% and 8% of V , whereas V=1/60 seconds. If the width is taken to be the maximum value of 0.08V (1.33 ms) then this blanking time is long enough to include 21 horizontal scanning lines of width H (63.5 μs). Therefore 21 lines are blanked out during each field or 42 lines per frame. Figure 4.6 provides a better understanding of the vertical blanking period. Immediately after the last horizontal line, the vertical blanking pulse brings the voltage to black level as shown in Figure 4.6. The vertical blanking period begins with a group of six equalizing pulses with half-line interval spacing, then the vertical sync pulse with six serrations at half-line intervals, which makes the complete vertical sync three lines wide. Following the sync pulse is another set of six equalizing pulses and a train of horizontal syncs. Notice the time interval between the first equalizing pulse and the last horizontal sync (before blanking occurs). In the first field it is equal to a scanning line width while in the second field it has a half-line value. This half-line difference is essential in maintaining the timing for odd-line interlacing. This difference continues for all successive fields. The timing details of the vertical blanking period are summarized in Table 4.3.
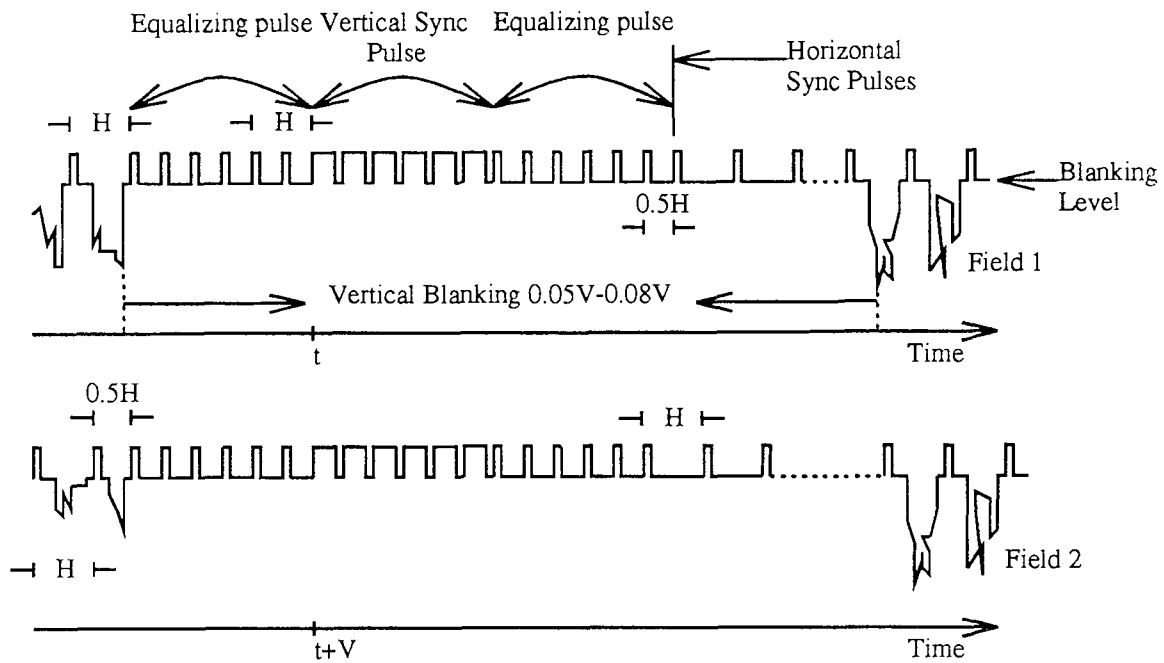
Figure 4.6 Vertical Blanking and Sync Pulses.

Table 4.3 Details of Vertical Blanking.

Period	Time
Total field	V 1/60 s
V blanking	0.05-0.08 V
Each V sync pulse	H/2
Each E pulse	0.04H
Each serration	0.07H
Visible field time	0.92-0.95V

A video signal consists of the continuous amplitude variation for individual pixels and a DC component corresponding to the average brightness

in the scene. This added signal is needed by the receiver to follow variations in the brightness. For instance, a gray element on a black background will have the same signal as a white element on gray background if no average brightness information is included. The required dc component of the video signal is its average value for each complete frame, since the background information indicates the brightness of the scene.

CHAPTER 5

MINIMUM RESOLVABLE TEMPERATURE DIFFERENCE

The standard performance evaluation of a thermal imager typically consists of the minimum resolvable temperature difference parameter along with other figures of merit such as the noise equivalent temperature difference (NEΔT), Modulation Transfer function (MTF) and uniformity. The MRTD has been shown to be a good criterion in assessing the overall performance of an imaging system since it englobes both noise and MTF effects. It provides information about the temperature difference sensitivity and the spatial resolution of the camera part in the thermal imaging system under analysis.

5.1 Definition of MRTD

The MRTD concept is defined in terms of a standard experiment shown in Figure 2.1. The test setup consists of a target (involving a blackbody source, an ambient plate, a standard test pattern and the optics), the IR equipment under evaluation, and the eye-brain system of the observer. The test target displayed in Figure 2.1 (b) is a 4 bar pattern where each bar opening has a 7 to 1 aspect ratio [6]. Typically, four bar patterns at varying spatial frequencies are imaged in order to produce an MRTD curve, although in our study other bar pattern configurations (3 bars, 16 bars) were included as well.

34
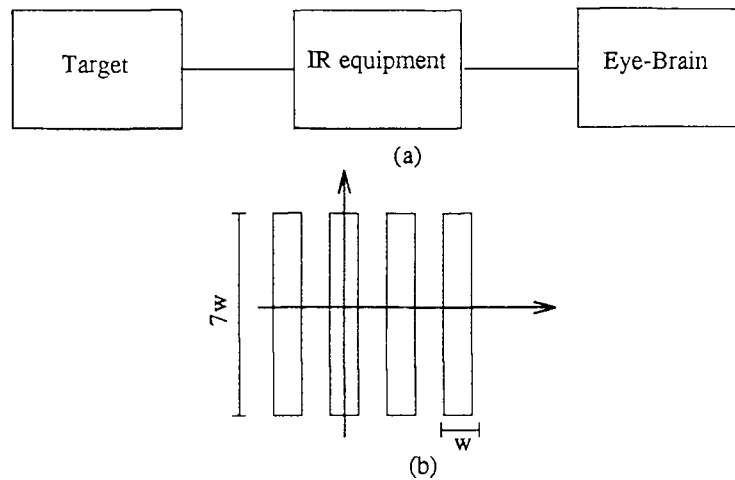
Figure 5.1 Block Diagram of the Standard MRTD Test Configuration.

The test consists of placing the test pattern at the focal place, and of varying the temperature difference ΔT between the test pattern and the ambient plate from an initial value of zero to a certain ΔT_f whereupon three out of four observers agree that the pattern is discernible. This ΔT_f is the MRTD value of the system at that spatial frequency. The same procedure is repeated for a number of patterns with different spatial frequencies. Finally, the MRTD curve is obtained by plotting ΔT_f as a function of spatial frequency (f).

5.2 Brief Literature Review

The two main thrusts of this area of investigation are on one hand the formal modeling of the hypotheses affecting the recognition of a particular scene, and on the other, the computer-aided objective determination. In the classical Ratches-Lawson model [6], it is hypothesized that the only limiting factor in recognizing a scene is its signal to noise (SNR) ratio. The test pattern

becomes recognizable when the SNR exceeds a certain threshold value SNR_{th}. The analytic modeling of the eye-brain system and the perception of the visual information has been the focal point of a good portion of the research into an objective determination of the MRTD . These models are based on the data from numerous experiments done to understand the behavior of the eye-brain system. The two main mechanisms identified are (a) optical response of the eye-lens considering the effects of diffraction and chromatic aberrations, and, (b) a biological response that enhances the SNR which can be modeled either as an adaptive matched filter or a synchronous integrator coupled with time integration.

The synchronous integrator model assumes that the eye integrates over an angular region defined by the target edges as imprinted on the retina. This angular region is represented as the target perimeter for high frequencies and an integration strip around each of the single bars when imaging low frequency patterns. Some well-correlated results were obtained by Vortman and Bar-Lev [7] with the limited synchronous model. The other model of the eye-brain couplet is the adaptive matched filter which by definition maximizes the SNR [8]. The signal and noise emitted by the display impinge on the eye retina after prefiltering by the eye lens, with the dominant incoming noise element due to the IR photon flux fluctuations, which although is white initially, has colored spectral characteristics at the monitor. This change in the noise is due to the response of the detector and the associated electronics.

Depending on which noise spectrum is assumed the matched filter will have significantly different expressions [7]. In [9] the authors describe an approach that appears to produce results well correlated with the subjective measurements at most spatial frequencies ranges. The method relies on the calculation of the system modulation transfer function, calculation of the noise power spectrum and modeling the eye-brain response as a filter function. The MRTD calculation based on these assumptions follows a semi-empirical formula given by

$$MRTD\ (f) = \frac{FN_s\ (f) * FF_e\ (f)}{MTF_s\ (f) * MTF_e\ (f)},$$

where FN_s is the noise power spectrum, FF_e is the filter function representing the eye-brain integration system and the system modulation function MTF_s is obtained by means of a Fourier transform of the measured line spread function. The eye MTF is given by

$$MTF_e(f) = sin^2\left[\frac{\pi}{2} \cdot \left(\frac{f}{f_m}\right)^{1/3}\right].$$

where f_m is the frequency of the maximum response of the eye reported to the object space.

In the same vein, Holst [10] reports an objective MRTD for digital scan-converted forward looking infrared (FLIR) systems using both calculated and measured MTFs (NVL equations) and NEΔT and using empirical data for the eye-brain modeling. Allowing the viewer to adjust his observation

distance, a certain optimization occurs whereby it results in an equal detection capability for all frequencies, i.e $MTF_{eye} \rightarrow$ constant. The MRT expression is simplified to:

$$MRT(f) = SNR_{th} \frac{NE\Delta T}{MTF_{sys}(f)\ MTF_{eye}(f)} = k \frac{NE\Delta T}{MTF_{sys}(f)}, \quad k = 0.7$$

Similar formulations are used in [11] and [12], with $k = 0.5$, and $0.5 < k < 1$.

5.3 Objective MRTD Measurement

The approach in this study is an adaptation of the work done by Williams et al. as described in [13] and [14]. The capability to detect a particular target is assumed to depend ultimately on bypassing some threshold SNR in the brain visual center. Williams established that the process of detection can be simulated instrumentally, with the premise that the eye-brain system behaves as though what it measures as signal corresponds to the difference between the total number of photons detected from the total target and the total number of photons from an equal area of background. The noise in this proposition is given by the RMS variation in the total number from either target or background over the integration time of the eye. The observer in essence is replaced by a visible camera viewing the target display and a signal processing system that can differentiate between the target and background pixels, and can measure the integrated signals as well as the RMS fluctuations in the average values of these signals. The overall setup used in [13] consists of the

thermal imaging system under test viewing an MRTD 4 bar pattern with the resulting visual image displayed. This image is in its turn viewed by a CCD FPA visible camera whose output is digitized, stored and processed in order to obtain a SNR corresponding to the temperature differential of the target.

5.3.1 Description of Setup

The main point in this project is to obtain some kind of relationship between the SNR of the thermal image itself and the MRTD at the corresponding frequency. The experimental setup used is shown in Figure 5.2. The thermal system under evaluation is the infrared camera discussed in [1], whose imager is the Sarnoff 2-D 320 X 244 IR CCD Focal Plane Array with platinum silicide Schottky barrier detectors (PtSi SBD). Each pixel size is 40X40 (μ m), with a 43 % optical fill factor. The camera is operating at 30 frames/s with a 100 mm focal length, 7 ° field of view and 1.4 f/# lens. The detection range is in the medium wave IR region bounded by $\lambda_o = 3.4$, $\lambda_f = 5.6$ μm. The camera is viewing the periodic bar target whose temperature and that of the background is set by a temperature source, with an accuracy of $\pm 0.03°$C, and an emissivity of 0.99% $\pm$ 0.01. The temperature source is remotely controlled through a serial connection (RS-232-C) to the computer used [1].

---

[1] See Appendix B

The image processing part is handled by Datacube's MaxVideo boards connected on the VMEbus to the workstation. The three boards used in the real-time acquisition system are the following MaxVideo modules:

• Input board: MAX-SCAN

• Frame processing board: ROI-STORE

• Output board: MAX-GRAPH
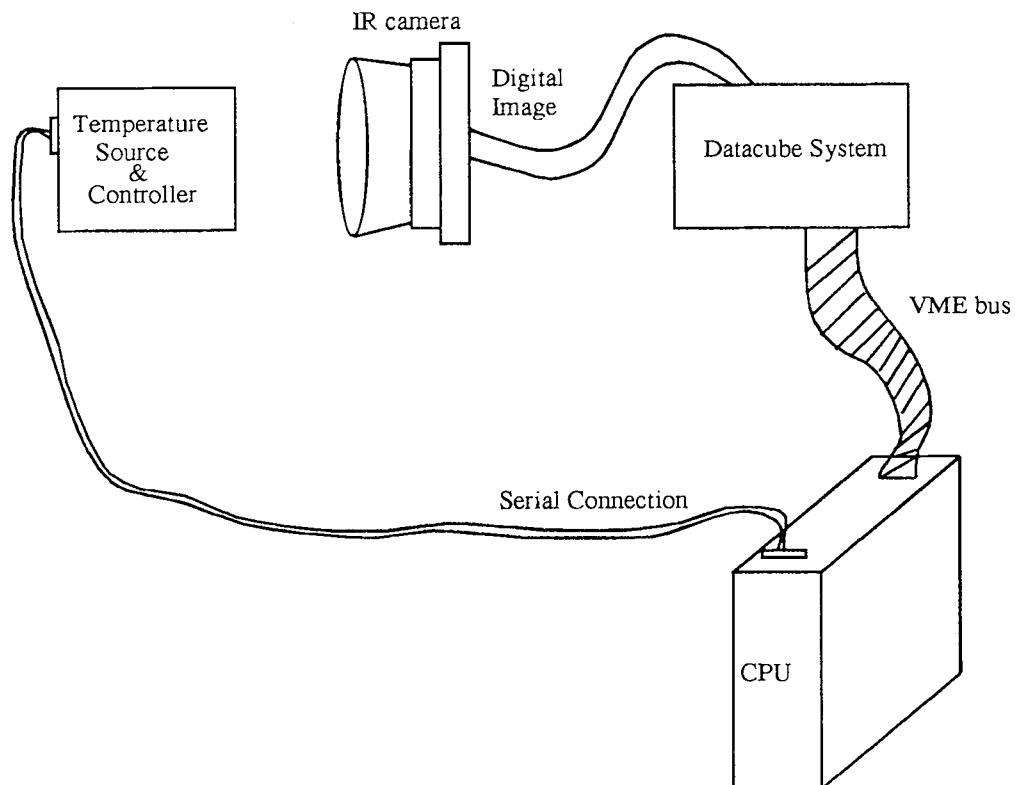
Figure 5.2 Objective MRTD Test Setup Configuration.

5.3.1.1 Datacube Interface MAX-SCAN is a programmable asynchronous input module which can acquire either analog or digital input data with a wide range of resolutions and frame rates. For details on the architecture of this module please refer to MAX-SCAN user's manual Revision 2.0 ©. This board is configured in the following mode:

- Digital input of 12 bits at 6.5 MHz converted to 10 MHz 16 bit MAXbus output data.

- External pixel clock,horizontal and vertical sync signals.

- ROI (region of interest) Timing master.

The MAX-SCAN was programmed to acquire an entire image frame with all necessary timing signals generated by the IR camera. All digital bits and timing signals were connected to the P11 digital port. Since the P11 connector has 16 pins assigned for digital data, the pins corresponding to the lower 4 bits were grounded. The images corresponding to the lower and higher bytes were acquired through the MaxVideo primitives and then were manipulated to produce 12 bit frames. Obviously, only the 8 bit images were displayed to check the good functioning of the software. The ROI-STORE board was programmed to acquire the entire frame (even and odd fields) in interlace mode. The ROI-STORE program used was similar to the sample source code provided by Datacube for the acquisition of RS-170 video.

5.3.2 Algorithm Implemented

The steps leading to the calculation of the MRTD are summarized below:

• A bitmask corresponding to the target and background pixels is calculated

from a high temperature difference $\left| \Delta T_{target} - \Delta T_{background} \right|$ frame. The image

obtained contains three different areas as shown below, a target, background

and surrounding areas. The boundaries of the surround area is delimited

visually through an image viewing utility. The bitmask is evaluated by

means of a thresholding criteria. An edge-detection procedure using Sobel

operators was tried out but was found to be less desirable then the threshold-

ing option. Thresholding is optimal because in effect the high temperature

difference image is a bi-level one. A typical resulting histogram is shown in

Figure 5.3(b).
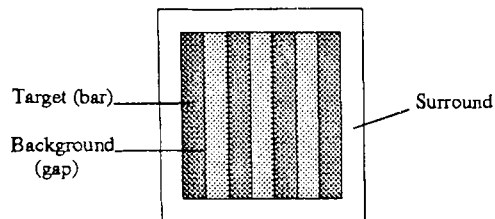
Figure 5.3 (a) Establishing a Bitmask from the Selected Image.
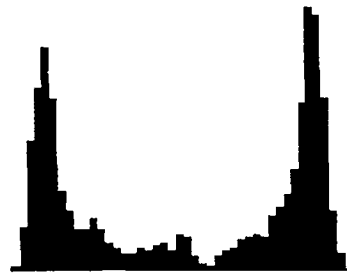
Figure 5.3 (b) Resulting Histogram for a Difference of 15° C.

• The temperature difference is reduced to a value close to the expected MRTD for the chosen spatial frequency. At this temperature, the image is acquired.

• The bitmask of the pattern is used to compute the bar and gap irradiance statistics (mean and standard deviation) needed for the SNR formula given by

$$SNR = 2 \frac{\left[\overline{S_{bar}} - \overline{S_{gap}}\right]}{\left[\sigma_{S_{bar}} + \sigma_{S_{gap}}\right]} .$$

(5.1)

where $S_{bar,gap}$ is the total signal at the detector.

• The SNR at that temperature is compared to the set threshold value. If it equals this SNR_{th} within a specified tolerance then the temperature at that point is the MRTD of the pattern at that spatial frequency. Otherwise a new temperature is set. Since the accuracy of the temperature controller is ±0.03 then the minimum temperature is set to 0.06, and is incremented by 0.06 over a range of temperatures, until some set threshold is reached.

•SNR_{th} ± (Δ_{SNR} = 0.06)

Initially, a set of images were captured and analyzed, and from the gathered data compared to the available subjective MRTDs, an attempt to deduce a threshold signal to noise ration was made.

5.3.3 Derivation of Applied SNR Formula

The IR camera electronics produces a voltage output which is directly proportional to the signal S integrated by the detector, thus the following relationship holds true,

$$G = K_1 S + K_2 .$$ (5.2)

Where G denotes the resulting gray level of the digitized image, K_1 is the overall gain of the system and K_2 is its offset. Since this is a linear relationship, the statistics of G can be expressed in terms of the mean and variance of S. Applying the expected value definition to equation (5.2) yields the following relationships:

$$\bar{G} = K_1 \bar{S} + K_2 .$$

$$\sigma_G^2 = E[G^2] - \bar{G}^2 = K_1^2 \sigma_S^2 .$$

Therefore the SNR can be obtained from a calculation based on the gray level equivalent, which after the appropriate substitutions is expressed as :

$$SNR = 2 \frac{\left[\overline{G_{bar}} - \overline{G_{gap}} \right]}{\left[\sigma_{G_{bar}} + \sigma_{G_{gap}} \right]} .$$ (5.3)

K_1 does not appear in the gray level equivalent SNR. If K_1 is needed, it can be estimated experimentally by a simple procedure, where two images are taken of the blackbody target set at two different temperatures. This operation produces two sets of data, where all things being equal, the offset

and the gain remain unchanged:

$$G_1 = K_1 S(T_1) + K_2 ,$$

$$G_2 = K_1 S(T_2) + K_2 .$$

The offset and the gain terms have a geometrical dependence in both the x and y directions to account for the imager's nonuniformity but for practical purposes it is replaced by an average value.

$$\overline{K_1} = \frac{\overline{G_1} - \overline{G_2}}{S(T_1) - S(T_2)} .$$

The amount of radiation incident at the detector is very dependent on the solid angle through which the detector sees the source. Solid angles are an extension of the plane angles to three dimensions [2]. The irradiance at the detector plane is given by the following equation derived in section 3.2.3:

$$E = \frac{LA_1}{f^2} \cos^4 \theta .$$

Where L is the sterance of the source, f is the focal length of the lens A_1 is the area of the lens and θ is the off-axis angle between lens and detector. Substituting $A_1 = \pi D^2/4$ in the above equation yields:

$$E = \frac{\pi L}{4(f/\#)^2} \cos^4 \theta . \tag{5.4}$$

---

[2] See Chapter 2 for details.

where f/# is defined as f/D. Our particular lens system has a field of view of 7° which makes the cosine term → 1. The previous expression defines the incident photon flux at the detector plane. It should be noted that L and E have a temperature and spectral dependence, even though the notation of equation (5.4) suppresses it. The integrated signal by each PtSi SBD in A/cm^2 is related to the irradiance E at the detector by the present integral:

$$S = \int_{3.4}^{5.6} R(\lambda)E(\lambda, T)d\lambda$$

where $R(\lambda)$ is the PtSi SBD responsivity and the photon irradiance is given through equation (5.4). The detector's responsivity in A/W is measured experimentally and can be approximated by a Fowler equation [15]

$$R(\lambda) = C_1[1 - \frac{\psi_{ms}\lambda}{1.24}]^2 . \tag{5.5}$$

where

C_1: the quantum efficiency coefficient equal to 0.2671 eV^{-1},

ψ_{ms}: the metal-semiconductor Schottky barrier detector (= 0.2199 eV),

λ: the wavelength of the infrared radiation in μm

Since the irradiance is given in $q \cdot sec^{-1} \cdot cm^{-2}$, the responsivity units need to be converted. When the signal source is a perfect emitter then the following must hold over the entire spectrum:

$$\sigma_e T^4 \left[W \cdot cm^{-2} \right] = k\sigma_q T^3 \left[q \cdot sec^{-1} \cdot cm^{-2} \right] .$$

which gives a conversion factor k defined as $k = \frac{\sigma_e}{\sigma_q} T$ in $\left[W/q \cdot sec^{-1} \right]$

which will be used in the R(λ) expression in order to get the photon-flux units. Figure 5.4 is a plot of the signal in e⁻/pixel versus temperature. In the final expression the detector area, fill factor, time integration and electron charge are introduced to the signal formulation:

$$S = A_d \times ff \times t \int_{3.4}^{5.6} R(\lambda)E(\lambda, T)d\lambda$$
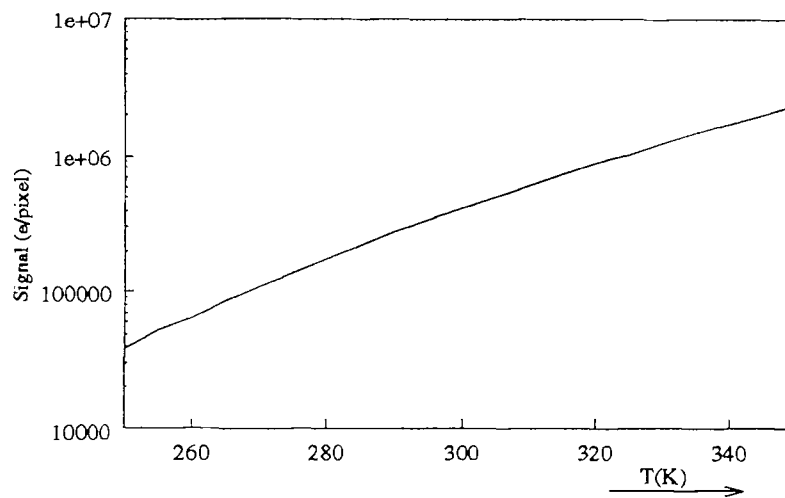
Figure 5.4 Integrated Signal per Pixel at Room Temperatures.

5.3.4 Results

The MRTD curve is a plot of temperature versus spatial frequency, which is defined with the help of Figure 2-5, as

$$\zeta = \frac{R}{X} = \frac{1}{\theta} \quad \text{[cycles/radians]}$$
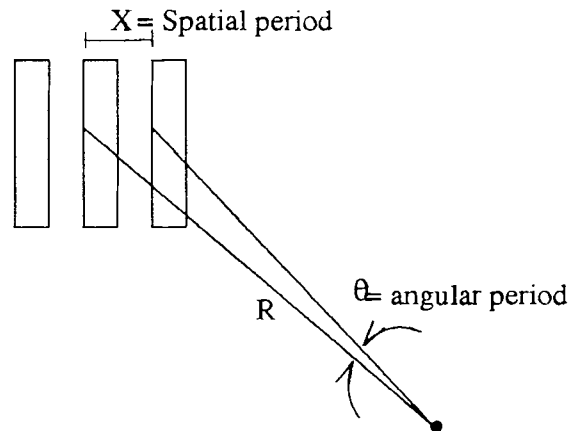
Figure 2.5 Angular Spatial Frequency.

following the algorithm expanded on in a previous section, the SNR corresponding to various temperature differences (ΔT) is evaluated for the following set of angular spatial frequencies,

$$\zeta_1 = 0.084\text{cy/mrad} \ , \ \zeta_2 = 0.148\text{cy/mrad}$$

$$\zeta_3 = 0.194\text{cy/mrad} \ , \ \zeta_4 = 0.42\text{cy/mrad}$$

$$\zeta_5 = 0.068\text{cy/mrad} \ , \ \zeta_6 = 0.336\text{cy/mrad}$$

Figures 5.6 (a) through (e) represent the SNR as a function of temperature, and at successively higher frequencies. It was found that the 12 bit images were excessively noisy, being in essence the higher 8 bits with the addition of a very noisy nibble. The least significant byte images, when displayed are noisy such that no pattern is discernible until a very high $\Delta T = 25°C$ is reached, for even small spatial frequencies.
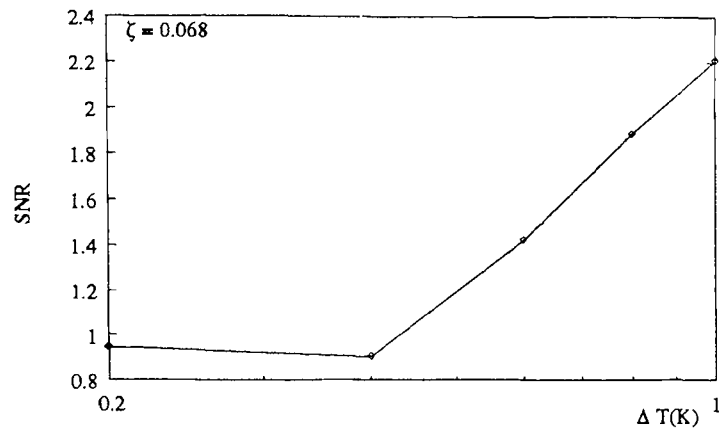
(a) SNR vs ΔT at $\zeta = 0.068$ cy/mrad.
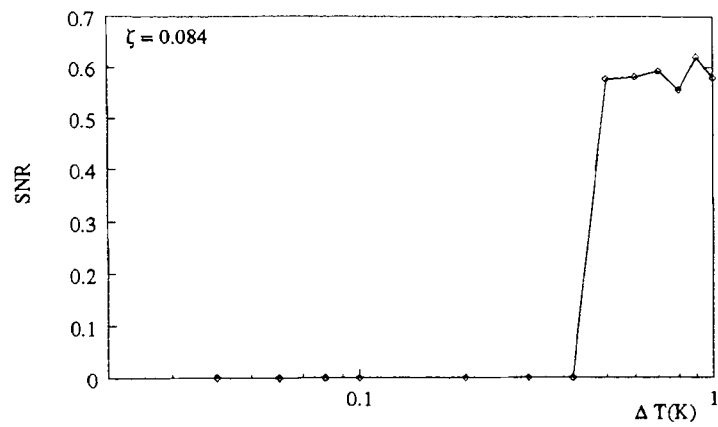
(b) SNR vs ΔT at $\zeta = 0.084$ cy/mrad.
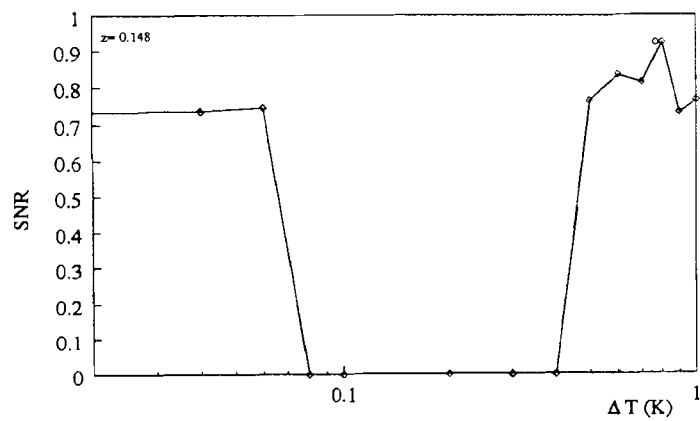
(c) SNR vs ΔT at $\zeta = 0.148$ cy/mrad.
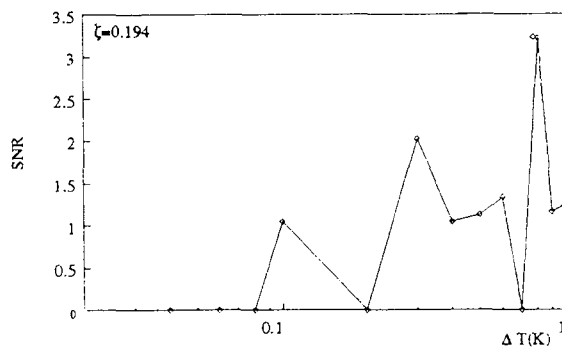
(d) SNR vs ΔT at $\zeta = 0.194$ cy/mrad.
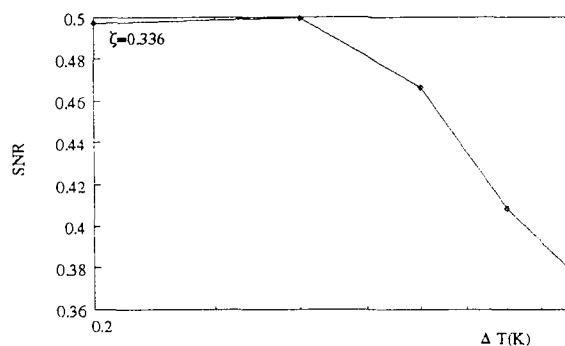
(e) SNR vs ΔT at $\zeta = 0.336$ cy/mrad.

Figure 5.6 Plots of SNR vs T at Various Frequency Values.

The subjective MRTD curve calculated in [1] was used, at this stage, to try to determine a certain signal to noise ratio threshold.
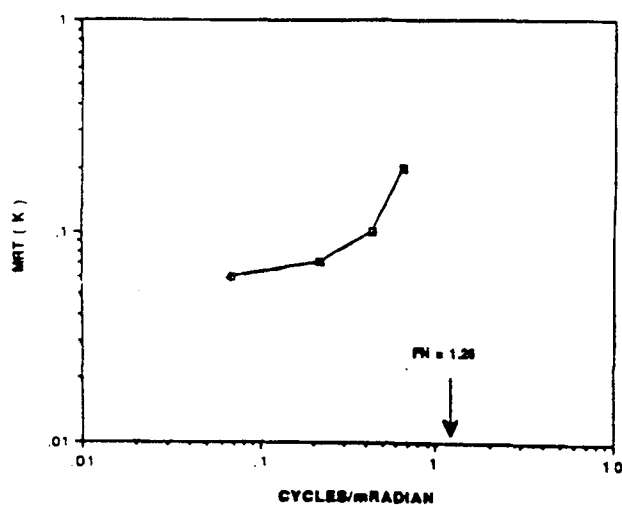
Figure 5.7 Subjective MRTD Curve.

5.3.5 Discussion of Results

What is evident from the previous curves is that at high frequencies, the calculated signal to noise ratio exhibits some unexplainable features. At $\zeta = 0.336$ cy/mrad, the displayed function decreases with increasing temperature, which can be explained in terms of the limited resolution of the optical system, which causes a "filling in" of the gaps, and this decreases the modulation depth in the image relative to that in the object. Although the loss in resolution exists at all frequencies it is more evident at the higher range because of the smaller details desired.

The inconsistencies of the obtained data does not allow a global assignment of a threshold SNR corresponding to an MRTD. It is possible to assign a threshold value for the lower frequencies, for instance at $\zeta = 0.148$ cy/mrad, which lies in the midrange of the frequencies investigated. The signal to noise ratio shows a marked transition from one phase to another suggesting the applicability of the SNR_{th}. For a value lying at the midpoint of the transition, $SNR_{th} = 0.4$, the corresponding temperature difference is very close to the subjective MRTD value. It is important then to look at the possible explanations of the inconsistencies, in order to either eliminate its sources or to develop a certain correction factor that will be added to the signal to noise formulation used in this project.

In the development of the algorithm it is assumed that the ambient environment does not vary from one set of experiments to the next. The

fluctuations of the environment, i.e the ambient temperature and the amount of signal integrated by the imager at that temperature could lead to erroneous results. Another avenue for the introduction of errors is the visual method used to delineate the pattern (bars and gaps). In retrospect, a modification of the thresholding criteria could have been used to achieve the same effect if not a more accurate "pattern grabbing". As far as the instrumentation errors, the temperature controller of the blackbody source has a display resolution of $\pm 0.01°C$ and a stability of $\pm 0.01°C$ which is a problem when the temperature difference is of the same order as the margins of uncertainties. Another simplification done throughout is considering the off-axis angle subtended by the detector at the lens to be negligible, and considering the lens to be free of aberrations such as coma. In summary, the errors are two-fold: geometrical optics simplification and instrumentation inaccuracies, both of which can be corrected.

CHAPTER 6

CONCLUSION

As part of this project a real-time digital image acquisition system using the Datacube MaxVideo boards and MaxWare primitive functions as a software basis was developed. This image acquisition software can be modified to accept frames of different sizes for future applications, as well as using it to implement various real-time image processing features, such as frame averaging.

Software was developed for the calculation of signal to noise ratio for four bar patterns used in MRTD measurements. It appears that the algorithm used for these computations was not effective at low spatial frequencies, due to noise sources associated with electrical pickup. At the end of the project, the interconnection between the Datacube system and the IR camera has been improved by means of fiber optic couplers. This improved new system will be the workbench for further work in this subject.

Experimental MRTD measurements performed were found to be consistent with previousdata reported by M. Patel [1]. However, more work is still needed before a definite conclusion can be made on the correlation between the experimental MRTD values and the corresponding calculation of signal to noise ratio.

53

APPENDIX A

BLACKBODY EXCITANCE TABLES AND

NUMERICAL ROUTINES

Table A.1 contains the values of the integral of the photon-flux

excitance: $\int_0^{\lambda_p} M_p(\lambda, T) \, d\lambda$ $\left[\text{photons sec}^{-1}\text{cm}^{-2}\right]$, $1.00 \leq \lambda_p(\mu m) \leq 100$

Table A.1 Values of integrated photon-flux excitance at various temperatures.

Wavelength (microns)	Temperature (K)					
	200	273	293	300	400	500
1.00	1.53E-10	4.78E-02	1.88E+00	6.05E+00	1.32E+06	2.22E+09
1.50	4.60E+00	1.72E+06	1.90E+07	4.09E+07	1.28E+11	1.70E+13
2.00	2.44E+05	4.09E+09	2.57E+10	4.63E+10	2.33E+13	1.07E+15
2.50	1.60E+08	4.53E+11	2.05E+12	3.31E+12	5.45E+14	1.25E+16
3.00	1.25E+10	1.05E+13	3.76E+13	5.66E+13	4.27E+15	6.11E+16
3.50	2.81E+11	9.63E+13	2.91E+14	4.15E+14	1.79E+16	1.83E+17
4.00	2.83E+12	4.93E+14	1.31E+15	1.80E+15	5.08E+16	4.05E+17
4.50	1.67E+13	1.72E+15	4.15E+15	5.50E+15	1.12E+17	7.36E+17
5.00	6.79E+13	4.57E+15	1.02E+16	1.32E+16	2.07E+17	1.17E+18
5.50	2.10E+14	1.00E+16	2.10E+16	2.66E+16	3.38E+17	1.69E+18
6.00	5.33E+14	1.91E+16	3.79E+16	4.72E+16	5.04E+17	2.27E+18
6.50	1.16E+15	3.25E+16	6.18E+16	7.60E+16	7.00E+17	2.89E+18
7.00	2.23E+15	5.10E+16	9.33E+16	1.13E+17	9.21E+17	3.54E+18
7.50	3.91E+15	7.48E+16	1.32E+17	1.59E+17	1.16E+18	4.19E+18
8.00	6.35E+15	1.04E+17	1.79E+17	2.13E+17	1.42E+18	4.85E+18
8.50	9.67E+15	1.38E+17	2.32E+17	2.74E+17	1.68E+18	5.49E+18
9.00	1.40E+16	1.77E+17	2.90E+17	3.41E+17	1.95E+18	6.11E+18
9.50	1.94E+16	2.20E+17	3.54E+17	4.13E+17	2.21E+18	6.71E+18
10.00	2.59E+16	2.67E+17	4.23E+17	4.90E+17	2.48E+18	7.29E+18
10.50	3.36E+16	3.18E+17	4.94E+17	5.70E+17	2.74E+18	7.83E+18
11.00	4.23E+16	3.70E+17	5.68E+17	6.52E+17	3.00E+18	8.35E+18
11.50	5.22E+16	4.25E+17	6.44E+17	7.36E+17	3.25E+18	8.85E+18
12.00	6.30E+16	4.81E+17	7.20E+17	8.21E+17	3.50E+18	9.32E+18
12.50	7.48E+16	5.39E+17	7.98E+17	9.06E+17	3.73E+18	9.76E+18
13.00	8.75E+16	5.97E+17	8.75E+17	9.91E+17	3.96E+18	1.02E+19
13.50	1.01E+17	6.55E+17	9.52E+17	1.07E+18	4.17E+18	1.06E+19
14.00	1.15E+17	7.13E+17	1.03E+18	1.16E+18	4.38E+18	1.09E+19
15.00	1.45E+17	8.29E+17	1.18E+18	1.32E+18	4.77E+18	1.16E+19
16.00	1.77E+17	9.42E+17	1.32E+18	1.47E+18	5.13E+18	1.22E+19
17.00	2.10E+17	1.05E+18	1.46E+18	1.62E+18	5.45E+18	1.28E+19
18.00	2.43E+17	1.15E+18	1.59E+18	1.76E+18	5.74E+18	1.32E+19
19.00	2.77E+17	1.25E+18	1.71E+18	1.89E+18	6.01E+18	1.37E+19
20.00	3.10E+17	1.35E+18	1.82E+18	2.01E+18	6.26E+18	1.41E+19
21.00	3.43E+17	1.43E+18	1.93E+18	2.13E+18	6.48E+18	1.44E+19
22.00	3.75E+17	1.52E+18	2.03E+18	2.23E+18	6.68E+18	1.47E+19
13.00	8.75E+16	5.99E+17	8.78E+17	9.93E+17	3.96E+18	1.02E+19
24.00	4.37E+17	1.67E+18	2.21E+18	2.42E+18	7.04E+18	1.53E+19
25.00	4.66E+17	1.74E+18	2.29E+18	2.51E+18	7.20E+18	1.55E+19
26.00	4.94E+17	1.80E+18	2.37E+18	2.59E+18	7.34E+18	1.57E+19
27.00	5.21E+17	1.86E+18	2.44E+18	2.66E+18	7.47E+18	1.59E+19
28.00	5.47E+17	1.92E+18	2.50E+18	2.73E+18	7.59E+18	1.61E+19
29.00	5.72E+17	1.97E+18	2.56E+18	2.80E+18	7.71E+18	1.62E+19
30.00	5.96E+17	2.02E+18	2.62E+18	2.86E+18	7.81E+18	1.64E+19
35.00	7.00E+17	2.23E+18	2.86E+18	3.11E+18	8.23E+18	1.70E+19
40.00	7.82E+17	2.39E+18	3.04E+18	3.29E+18	8.53E+18	1.74E+19
45.00	8.47E+17	2.50E+18	3.17E+18	3.43E+18	8.75E+18	1.77E+19

This table is readily calculated using numerical integration routines varying in speed and relative error. The source code listed in the next pages tested the trapezoidal rule, Simpson's integration method, adaptive quadrature and Romberg's algorithm.

A.1 Numerical Integration Routines

```
#include <math.h>

#include <stdio.h>

double intsimp();

double f();

double adapt();

double trap();

double romberg();

double tolerance;

double Temp,

    PI,

    C,

    H,

    K,

    B,

    CONS;

main(argc, argv)
```

```c
int argc;

char *argv[];

{

double rom,lambda,M;

int iterations,i;

FILE *fd;

if (argc <= 1)

    {

    printf("%s 0,"a.out Temperature ");

    exit(-1);

    }

tolerance = 1.0E-14;

PI = 4.0 * atan(1.0);

C = 2.99792438E+14; /*micrometer/sec*/

H = 6.626176e-34;   /*Joules.sec*/

K = 1.380662E-23;   /*Joules/Kelvin*/

Temp = atof(argv[1]); /*Kelvin*/

iterations = 10;

B = (H * C) / (K * Temp);

CONS = 2*PI*C;

fd = fopen ("int", "w+");

for (lambda=0.1; lambda <40.0 ; lambda = lambda+0.1)
```

```
{

rom = romberg(1e-16, lambda ,iterations );

fprintf(fd," %f%16.4lf0, lambda,CONS*rom*1e+08);

}

}
```

/**/

```
double intsimp(a,b,N)

double a, b;

int N;

{

register int i;

register double w, s;

s = 0.0;

w = (b-a) / N;

for(i=0; i<N; i++)

   s = s + w * (f(a+((double)i-1.0)*w) + 4.0 * f(a-w/2.0

   +(double)i*w) + f(a+(double)i*w)) /6.0;

return (s) ;

}
```

/**/

```
double f(lambda)

double lambda;
```

```
{

double fun;

fun =  (pow(lambda, -4.0) / (exp(B/lambda) -1.0))   ;

return (fun);

}
/***************************************************/
double adapt(a,b)

double a,b;

{

 if( fabs(intsimp(a,b,20) - intsimp(a, b, 10)) < tolerance)

   return ( intsimp(a, b,20));

 else

   return ( adapt(a,(a+b)/2.0) + adapt((a+b)/2, b));

}
/***************************************************/
double trap(a, b, n)

double a,b;

int n;

{

double h, sum;

int i;

h = (b-a)/(n-1);
```

```
sum = (0.5) * ( f(a) + f(a+(n-1)/h));

for (i=2; i<=n-1; i++)

  sum += f(a+ (i-1)*h);

sum *= h;

return (sum);

}
```

/***/

```
double romberg(a, b, N)

double a, b;

int N;

{

double R[500][500];

double h, sum;

int l, i, j, k,m;

h = b - a;

R[1][1] = 0.5 * h * (f(a) + f(b));

l= 1;

for (i=2; i<=N; i++)

  {

    h = 0.5 *h;

    l = l + l;

    sum = 0;
```

```
for(k=1;  k<= l-1; k+=2)

  sum += f(a + (double)k * h);


R[i][1] = 0.5*R[i-1][1] + h * sum;

m = 1;

for(j=2; j<= i; j++)

  {

    m = 4 * m;

    R[i][j] = R[i][j-1] + (R[i][j-1] - R[i-1][j-1])/(double)(m-1);

  }

}

return(R[N][N]);

}
```

APPENDIX B

RS-232-C INTERFACE

The blackbody source used in the experimentation necessary for this thesis is remotely controlled via an RS-232-C connection (DB-25). A menu-driven controller was written in C, implemented using UNIX supplied routines, which give the user a terminal-independent method of updating screens with reasonable optimization.

B.1 RS-232-C Physical Attributes

Figure B.1 describes the pins needed to establish communication between the temperature controller and the computer.

Computer   Temperature Controller
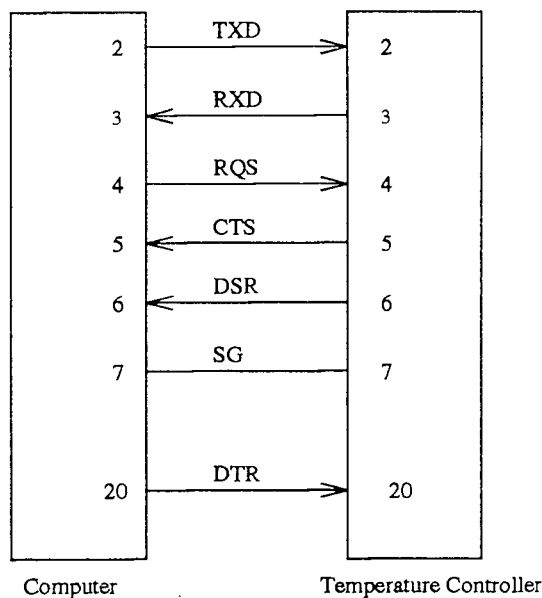
FigureB.1 RS-232 Connectors Pin Assignment

- TXD and RXD are the data lines in the directions indicated by the arrows.

- Line 7 carries the ground signal (SG).

- Line 6 carries a handshaking signal which is set by the temperature controller as an indication of its presence.

- Line 5 is used by a Clear To Send (CTS) signal set to high to indicate that the controller is ready to receive.

- The Request to Send (RQS) signal is on line 4 which is set to high by the computer to indicate its readiness to accept data.

The RS-232-C standard provides the following characteristics of the electrical signals used in direct serial connections. There are two allowed states:

SPACE corresponding to binary 0, whenever a positive voltage exists.

MARK corresponding to binary 1 , whenever a negative voltage exists.

On data lines (lines 2 & 3) a positive voltage corresponds to a logical 0 and a negative voltage to a logical 1. On handshaking lines (e.g., DTR,DSR). The positive voltage indicates that the line is on, thus enabling transmission, while a negative voltage halts the data flow. Positive voltage levels lie between +5 and +15 V for outputs, and between +3 and +15 for inputs. Negative voltages are set between -5 and -15 V for outputs and between -3 and -15 V for inputs. The difference in voltage specifications is meant to

compensate for the attenuation due to cable lengths.

B.2 Communication Program Source Listing

```c
#include <curses.h>

#include <fcntl.h>

#include <errno.h>

#include <termio.h>

#include <string.h>

void end_menu(n,m)

int  n,m;

{

    int y,x;

    wclear (stdscr);

    wattron(stdscr,A_STANDOUT);

    x=(int)m/4;

    y=(int)n/4;

    mvwaddstr(stdscr,y+10,x+5,"exiting driving program");

    wrefresh(stdscr);

    sleep(1);

    return;

}

char *input()
```

```
{
    int n,fd;

    struct termio set;

    char buf[1024];

    fd=open("/dev/ttya",O_RDWR);

    set.c_cflag &= ~CBAUD;

    set.c_cflag |= B75;

    set.c_cflag &= ~CSIZE;

    set.c_cflag |= CS8;

    set.c_cflag |= CLOCAL;

    set.c_cflag |= CREAD;

    set.c_cflag &= ~PARENB;

    set.c_iflag |= IGNCR;

    ioctl(fd,TCSETA,&set);

    sleep(6);

    n=read(fd,buf,200);

    sleep(6);

    n=read(fd,buf,200);

    close (fd);

    return buf;
}/*end of input*/
void output(delta)
```

```
char delta[10];

{

    struct termio set;

    char buf[100];

    int fd;

    fd=open("/dev/ttya",O_RDWR);

    set.c_cflag &= ~CBAUD;

    set.c_cflag |= B75;

    set.c_cflag &= ~CSIZE;

    set.c_cflag |= CS8;

    set.c_cflag |= CLOCAL;

    set.c_cflag |= CREAD;

    set.c_cflag &= ~PARENB;

    set.c_oflag &= ~OPOST;

    ioctl(fd,TCSETA,&set);

    buf[0]='D';

    strcat(buf,delta);

    strcat(buf,"");

    write(fd,buf,strlen(buf));

    close (fd);

    return;

}/*end of output*/
```

```
void main_menu(n,m)

int n,m;

{
    int y,x;

    char ch;

    y=(int)n/2;

    x=(int)m/4;

    box(stdscr,ACS_VLINE,ACS_HLINE);

    wattron(stdscr,A_STANDOUT);

    mvwaddstr(stdscr,y-3,x,"This menu drives the blackbody source");

    mvwaddstr(stdscr,y+3,x+5,"Press any key to continue");

    ch=wgetch(stdscr);

    wrefresh(stdscr);

    wattrset(stdscr,0);

    wclear(stdscr);

    return ;
}
char menu_3(n,m)

int n,m;

{
    int y,x,yi,xi;

    char *input(),cc;
```

```
WINDOW *menu2;

y=(int)n/4;

yi=y;

x=(int)m/4;

xi=x;

wclear(stdscr);

wrefresh(stdscr);

menu2=newwin(5,m,y-2,0);

box(menu2,ACS_VLINE,ACS_HLINE);

mvwaddstr(menu2,2,10,"Settings are: ");

wrefresh(menu2);

waddstr(menu2,input());

wrefresh(menu2);

wattron(stdscr,A_STANDOUT);

mvwaddstr(stdscr,yi+10,xi-8," To main menu press return, to exit

completely press esc ");

echo();

cc=wgetch(stdscr);

wclear(menu2);

wclear(stdscr);

wattroff(stdscr,A_STANDOUT);

return cc;
```

```
}

char menu_2(n,m)

int n,m;

{

    int y,x,yi,xi;

    char delta[10],cc;

    WINDOW *menu2;

    y=(int)n/4;

    yi=y;

    x=(int)m/4;

    xi=x;

    wclear(stdscr);

    wrefresh(stdscr);

    menu2=newwin(5,m,y-2,0);

    box(menu2,ACS_VLINE,ACS_HLINE);

    mvwaddstr(menu2,2,15," Set the temperature differential  ");

    getyx(menu2,y,x);

    wattron(menu2,A_STANDOUT);

    mvwaddstr(menu2,y,x+5,"Delta T=");

    wrefresh(menu2);

    wgetstr(menu2,delta);

    output(delta);
```

```
wattroff(menu2,A_STANDOUT);

wattron(stdscr,A_STANDOUT);

mvwaddstr(stdscr,yi+10,xi-8," To main menu press return, to exit

completely press esc ");

echo();

cc=wgetch(stdscr);

wclear(menu2);

wclear(stdscr);

wattroff(stdscr,A_STANDOUT);

return cc;

}

void menu_1(n,m)

int n,m;

{

    int y,x;

    char ch,menu_2(),menu_3(),c;

    y=(int)n/4;

    x=(int)m/4;

    box(stdscr,ACS_VLINE,ACS_HLINE);

    mvwaddstr(stdscr,y,x,"1- Set the temperature differential");

    y=y+3;

    mvwaddstr(stdscr,y,x,"2- Read the current temperature settings");
```

```
y=y+3;

mvwaddstr(stdscr,y,x,"3- Exit the driver");

y=y+5;

wattron(stdscr,A_STANDOUT);

mvwaddstr(stdscr,y,x,"Select Option Number");

getyx(stdscr,y,x);

wattroff(stdscr,A_STANDOUT);

mvwaddch(stdscr,y,x,' ');

ch=getch();

wrefresh(stdscr);

switch(ch){

case '1': do

        c=menu_2(n,m);

      while(c!=' 12'&& c!=' 33');

      if (c==' 12')

        menu_1(n,m);

      if (c==' 33')

        end_menu(n,m);

      break;

case '2': do

        c=menu_3(n,m);

      while(c!=' 12'&& c!=' 33');
```

```
            if (c==' 12')

                menu_1(n,m);

            if (c==' 33')

                end_menu(n,m);

            break;

       case '3':wclear(stdscr);

                end_menu(n,m);

                break;

       default: menu_1(n,m);

       }

       return ;

}

main()

{

    int lines,columns,i;

    /* Initialization */

    initscr();

    noecho();

    main_menu(LINES,COLS);

    echo();

    menu_1(LINES,COLS);

    endwin();
```

```
    return 0;

}
```

APPENDIX C

SIGNAL TO NOISE ROUTINE

This program computes the signal to noise ratio of the bar pattern on a pixel to pixel basis with the bar and gap pixels found previously by a thresholding routine. It outputs a histogram of the pattern which can be displayed as well as computing the contrast of the image.

```
#include <stdio.h>

#include <math.h>

/*This program computes the signal to noise ratio of the bar pattern on a pixel

basis with the bar and gap pixels found previously by a thresholding routine */

int cut();

void histogram();

void statistics();

int Xinit,

    Yinit,

    Xfinal,

    Yfinal;

int pattern_size,patheight,patwidth;

#define HEIGHT 238

#define WIDTH  320
```

```
#define SIZE   HEIGHT*WIDTH

main(argc,argv)

int argc;

char *argv[];

{
    if (argc!=6)

      {
        printf("0ormat:  a.out infile Xinit,Yinit,Xfinal,Yfinal0);

        exit(-1);

      }

    Xinit = atoi(argv[2]);

    Yinit = atoi(argv[3]);

    Xfinal = atoi(argv[4])+1;

    Yfinal = atoi(argv[5])+1;

    patheight = Yfinal-Yinit;

    patwidth = Xfinal-Xinit;

    pattern_size = cut(argv[1]);

    histogram(pattern_size);

    statistics(patheight,patwidth);

}
int cut(filename)

char *filename;
```

```
{

    FILE *fo,*fp;

    unsigned char c;

    char Byte[HEIGHT][WIDTH];

    char Byte1[HEIGHT][WIDTH];

    int i,j;

    fo=fopen(filename,"r");

    fp = fopen("target","wb");

    for(j=0;j<HEIGHT;j++)

        for (i=0; i<WIDTH; i++)

            {

            c=getc(fo);

            Byte[j][i]=c;

            }

    for(j=Yinit;j<Yfinal;j++)

        for (i=Xinit; i<Xfinal; i++)

            {

            c=Byte[j][i];

            Byte1[j-Yinit][i-Xinit]=c;

            }

    for(j=0;j<Yfinal-Yinit;j++)

        for (i=0; i<Xfinal-Xinit; i++)
```

```
        {

        c=Byte1[j][i];

        putc(c,fp);

        }


    fclose(fp);

    fclose(fo);

    return ((Yfinal-Yinit)*(Xfinal-Xinit));

}

void histogram(size)

int size;

{

    FILE *ls,*fp, *hi;

    unsigned char c1;

    int i,j, grey_value[256],number;

    char *byte;

    char him[512][256];

    double mean;

    ls = fopen("target","r");

    fp = fopen("histo","w");

    hi = fopen("histogram", "wb");

    byte = (char *)malloc(size);
```

```
fread(byte,size,1,ls);

for(i=0;i<256;i++)

    grey_value[i]=0;

for(i = 0; i<size; i++)

  {

  c1 = byte[i];

  grey_value[(int)c1]++;

  }

for(i=0;i<256;i++)

  {

  fprintf(fp,"%d%ld0,i,grey_value[i]);

  }

number = 0;

mean = 0.0;

for (i=0; i<256; i++)

    mean= mean+grey_value[i]*i;

    number= number+grey_value[i];

mean=mean/number;

for (i=0; i<512; i++)

  for(j=0; j<256; j++)

    him[i][j]=(char)255;

for(i=0; i<256; i++)
```

```
        for(j=511; j>512- (grey_value[i]/4); j--)

          him[j][i] = (char)0;

      fwrite(him, 512*256, 1,hi);

      printf("%f0,mean);

      free(byte);

      fclose(ls);

      fclose(fp);

      fclose(hi);

      return;

}
void statistics(height,width)

int height,width;

{

      FILE *ls,*fbar,*fgap,*fcon,*fs_n;

      int i,j,pixgaps,pixbars,n,sum,pix[111][111];

      unsigned char c;

      double meanbar,meangap,SDbar,SDgap,contrast,Signal_Noise;

      ls   = fopen("target","r");

      fgap = fopen("gap","r");

      fbar = fopen("bar","r");

      fcon  = fopen("contrast","a+");

      fs_n  = fopen("signal_noise","a+");
```

```
fscanf(fbar,"%d",&pixbars);

fscanf(fgap,"%d",&pixgaps);

for (j=0 ; j<height ; j++)

    for (i=0; i<width ; i++)

        {

        c=getc(ls);

        pix[j][i]=(int)c;

        }

sum=0;

for (n=0; n<pixgaps; n++)

    {

    fscanf (fgap,"%d%d0,&j,&i);

    sum = sum+pix[j][i];


    }

meangap= sum/pixgaps ;

rewind(fgap);

fscanf(fgap,"%d",&pixgaps);

sum=0;

for (n=0; n<pixgaps; n++)

    {

    fscanf (fgap,"%d%d0,&j,&i);
```

```
        sum = (pix[j][i]-meangap)*(pix[j][i]-meangap) +sum;

    }

SDgap= ((double)sum/pixgaps) ;

SDgap= sqrt (SDgap);

sum=0;

for (n=0; n<pixbars; n++)

    {

    fscanf (fbar,"%d%d0,&j,&i);

    sum=sum+pix[j][i];

    }

meanbar= sum/pixbars ;

rewind(fbar);

fscanf(fbar,"%d",&pixbars);

sum=0;

for (n=0; n<pixbars; n++)

    {

    fscanf (fbar,"%d%d0,&j,&i);

    sum = (pix[j][i]-meanbar)*(pix[j][i]-meanbar) +sum;

    }

SDbar= ((double)sum/pixbars) ;

SDbar= sqrt (SDbar);

contrast = (meanbar-meangap)/(meanbar+meangap);
```

```
Signal_Noise = (2*(meanbar-meangap))/(SDbar+SDgap);

fprintf(fcon,"%9.6f0,contrast);

fprintf(fs_n,"%9.6f0,Signal_Noise);

fclose(ls);

fclose(fbar);

fclose(fgap);

return;

}
```

REFERENCES

1. Patel, M. "PtSi SBD 320 X 244-Element IR-CCD Camera System," M.S Thesis, NJIT (1990)

2. Nicodemus, F. E., ed. *National Bureau of Standards Self-Study Manual on Optical Radiation Measurements*. Out of print Government Printing Office document, now available from the National Technical Information Service (NTIS), U.S. Department of Commerce.

3. Vincent, J. D. *Fundamentals of Infrared Detector Operation and Testing*, John Wiley & Sons, (1989)

4. Dereniak, E. L. and D. G. Crowe. *Optical Radiation Detectors*, John Wiley & Sons, (1984).

5. Hansen, G. *Introduction to Solid State TV System, Color and Black and White*, Prentice-Hall , NJ, (1969)

6. Ratches, J. A. "Static Performance Model for Thermal Imaging Systems," Opt. Eng (15)6, 525-530 (1976).

7. Vortman, J. G., and A. Bar-Lev. "Improved Minimum Resolvable Temperature Difference for Infrared Imaging Systems," Opt. Eng 26(6), 492-498 (1987).

8. Gao, M. L., M. A. Karim and S. H. Zheng. "Device Nonspecific Minimum Resolvable Temperature Difference for Infrared Imaging Systems Characterization," Opt. Eng 29(8), 905-910 (1990).

9. de Jong, A. N., and S. J. M. Bakker. "Fast and Objective MRTD Measurement" in *Infrared Systems-Design and Testing*, Proc. SPIE 916 127-143 (1988).

10. Holst, G. C. "Minimum Resolvable Temperature Predictions, Test Methodology, and Data Analysis," in *Infrared Technology XV*, Proc. SPIE 1157, 208-218 (1989).

11. Williams, T. L. "Update on Objective MRTD Measurement," in *Infrared Imaging Systems: Design, Analysis, Modeling, and Testing*, Proc. SPIE 1309, 286-291 (1991).

12. McCracken W., and L. Wajsfelner. "MRTD as a Figure of Merit," in *Thermal Imaging*, Proc. SPIE 636, 31-35 (1986).

13. Williams, T. L., N. T. Davidson and S. Wocial. " Results of some Preliminary Work on Objective MRTD Measurement," in *Image Quality: An Overview*, Proc. SPIE 549, 44-49 (1985).

14. Williams, T. L. " Assessing the Performance of Complete Thermal Imaging Systems, " in *Infrared Technology and Applications*, Proc. SPIE 590, 172-175 (1985).

15. Cohen, J., J. Vilms, and R. J. Archer. Air Force Cambridge Research Labs. Report No. 68-0651 (1968).